Main Manuscript for

Dissecting the molecular origins of opalescence and phase separation in mAb formulations and their relation to aggregation

Inna Brakti[a,b,1], Samuel Lenton[a,1], Marco Polimeni [a,1], Hannes Ausserwöger[c], Rob Scrutton[c], Anette Henriksen[d], Nikolai Lorenzen[d], Martin Nors Pedersen[b], Jesper Søndergaard Marino[d], Fátima Herranz-Trillo[e], Ann E. Terry[e], Tuomas P. J. Knowles[c], Minna Groenning[b], Vito Foderà[a,*]

[a]Department of Pharmacy, University of Copenhagen, Copenhagen, Denmark 2100, [b]Biophysical Analysis, CMC Analytical Support, Novo Nordisk A/S, Måløv, Denmark 2760, [c]Yusuf Hamied Department of Chemistry, Centre for Misfolding Diseases, University of Cambridge, Cambridge, United Kingdom CB2 1EW, [d] Novo Nordisk A/S, Therapeutics Discovery, Novo Nordisk Park, Måløv 2760, Denmark, [e]MAX IV Laboratory, Lund University, Fotongatan 2, 224 84 Lund, Sweden

[1] These authors contributed equally

* Vito Foderà

Address: Department of Pharmacy, University of Copenhagen, Copenhagen, Denmark 2100

Phone: +4535336131

Email: vito.fodera@sund.ku.dk

Author Contributions :

I.B: Designed research, performed research, analysed data, wrote the paper**, S.L:** Designed research, performed research, analysed data, wrote the paper**, M.P:** Designed research, performed research, analysed data, wrote the paper**, H.A:** Designed research, performed research, analysed data, revised the paper**, R.S:** Performed research, analysed data, revised the paper**, A.H:** Designed research, performed research, analysed data, revised the paper**, M.N.P:** revised the paper**, J.S.M:** Revised the paper**, N.L:** Revised the paper**, F.H.T:** Contributed new reagents/tools**, A.E.T:** Contributed new reagents/tools, revised the paper**, T.P.J.K:** Contributed new reagents/tools**,** revised the paper**, M.G:**, Designed research, revised the paper, acquired funding**, V.F:** Designed research, wrote the paper, acquired funding

Competing Interest Statement: A.H, N.L, M.N, J.S.M and M.G are employees of Novo Nordisk A/S.

Classification: Biological Sciences, Biophysics and Computational Biology

This manuscript was deposited as a preprint on bioRxiv and made available under a CC-BY-NC-ND 4.0 International license. **doi:** https://doi.org/10.1101/2025.08.29.672998

Keywords: antibody development, patchy interactions, liquid-liquid phase separation, opalescence, aggregation

This PDF file includes:

Main Text
Figures 1 to 5
Supplementary information (Figures S1-S16, Table S1)

Abstract

Liquid-liquid phase separation (LLPS) and high opalescence are two self-association phenomena commonly encountered in monoclonal antibody (mAb) formulations. Because of their impact on colloidal stability, they are commonly avoided, due to a suspected link with aggregation and reduced product shelf-life. However, the molecular underpinnings and interrelation between these phenomena remain unclear, complicating predictions of their occurrence. By combining light and X-ray scattering techniques with microscopy and advanced microfluidic setups, we here report the delicate phase behavior of a model mAb, named mAb1. This is characterized by rapid clustering and LLPS in a narrow NaCl range, above which it transitions into an opalescent state devoid of micron-sized assemblies, yet retaining a similar interaction fingerprint. Using Monte Carlo simulations, we report that the macroscopic solution state of mAb1 is controlled by a positive patch, whose degree of charge screening determines whether LLPS or opalescence will take place. Specifically, neutralization of this patch via counterion interactions diminishes intermolecular repulsion and favors the concerted action of weaker dipole-dipole/hydrophobic interactions, amounting to the creation of a new solution phase, via LLPS. Further NaCl addition distributes ions more uniformly across the surface, attenuating these attractive interactions, leading to the dismantling of droplets while preserving solution opalescence. Finally, we show that LLPS and opalescence are decoupled from stirring-induced aggregation, challenging an unequivocal relationship between these phenomena.

Significance Statement

Tailoring formulations to maximize the stability of therapeutic antibodies is crucial for their development. This is complicated by their tendency for self-association at high concentrations, where increased opalescence and phase separation, that are thought to precede irreversible aggregation, are routinely observed. Here, we studied the molecular underpinnings of mAb opalescence versus liquid-liquid phase separation. We report the mechanisms determining the two phenomena and provide a foundation for their prediction, which may guide the rational development of mAb formulations. We further show that LLPS and opalescence can be decoupled from stress-induced aggregation. We hypothesize that excluding mAbs from the bulk solvent via LLPS may even be harnessed to enhance drug product stability.

Introduction

Since the approval in 1986 by the US Food and Drug Administration of the first monoclonal antibody (mAb) as a novel drug modality, their commercial success has been continuously expanding (1–4). Therapeutic mAbs are usually administered parenterally by intravenous infusion or subcutaneous (SC) injection. For chronic disease management, the latter approach is favored, as it improves patient adherence, by providing a less intrusive delivery method and the ease of self-administration (5–8). However, due to their large size and often limited potency, mAbs formulations can exceed 100 mg/mL to reach relevant doses in the small injection volumes imposed by the SC route (≈2mL) (8, 9). In these concentrated regimes, the probability of collisions between mAb molecules increases and can result in the formation of higher-order protein assemblies. This can have several consequences on solution properties such as increased viscosity (10), opalescence (11) liquid-liquid phase separation (LLPS) (12) and/or the formation of soluble/insoluble aggregates (13). Opalescence refers to increased light scattering as a result of reversible attractive interactions (14) and is associated with large concentration fluctuations in the vicinity of a phase transition boundary without macroscopic assembly as detected by light microscopy (11, 15). This leads to a bluish solution appearance, akin to an opal stone (11). LLPS, on the other hand, is a phenomenon in which attractive interactions between macromolecules outbalance solvent interactions and physically separate from the bulk solution into a discrete phase with liquid-like properties (16). This

results in macromolecules concentrating into droplets, forming the “dense” phase, surrounded by a macromolecule-depleted “dilute” phase (16). However, as the properties of the droplet interior can be inhomogeneous, the more inclusive term “phase-separation” is preferably employed, unless the liquid-like nature of the droplets is confirmed (17). Both opalescence and LLPS are reversible and dependent on solution conditions. Despite the solution factors inducing these phenomena being well-known, much less is known about the molecular mechanisms driving opalescence versus LLPS. This is complicated by the fact that pure opalescence and LLPS can be visually hard to distinguish. The latter involves the formation of a new phase, often witnessed as micron-sized droplets which are detectable via microscopy, while high opalescence can be observed without any large-scale assembly. In a drug development context, opalescence above a defined threshold is often avoided as it is commonly flagged as a precursor for LLPS (6). The latter is a concern for two reasons: (1) the delicate formation and dissociation of droplets, based on changes in temperature, excipients, protein concentration and incubation time complicates the development of proper control strategies during a product’s shelf-life and (2) it has been linked to aggregation (11, 18). LLPS-related aggregation is mostly reported for protein systems with some level of intrinsic disorder (19–23). This has often been observed as a liquid-to-solid transition within “aged” droplets (24). Moreover, the distinct environment provided by the droplet interface has been shown to serve as nucleation point for fibril formation for several intrinsically disordered proteins (17, 22, 25). The importance of this inherent property of many proteins was highlighted for the amyotrophic lateral sclerosis-related protein SOD1, whose exposure of disordered loops in the absence of zinc led to phase separation and subsequent fibril formation (23). Interestingly, while droplet interfaces have been demonstrated to spearhead aggregation, recent reports also point toward a shielding role of the droplet interior, emphasizing the double-edged nature of this phenomenon (26, 27). Concerning large, folded mAbs, Pantuso et al. hypothesized that the LLPS-induced partial unfolding of a mAb promoted crystal growth along the droplet surface (28). On the other hand, Bramham et al. observed that the structural integrity of another mAb was conserved upon LLPS formation and no changes in the aggregation profile were detected after storage at refrigerated conditions (4°C) after 28 days (29).

In this study we integrated light- and X-ray scattering and microscopy, to discriminate between mAb opalescence and LLPS. By combining these approaches with controlled microfluidic mixing, we accessed a wide design space to carefully monitor the progression of interactions underlying LLPS, as well as their inhibition. Using coarse-grained Monte Carlo (MC) simulations, we rationalized the microscopic differences between LLPS and opalescence in terms of molecular interactions leading to the two phenomena. Finally, we linked this fundamental study of the macroscopic manifestations of mAb self-assembly to effects on the physical stability under stress conditions to support future formulation studies of mAbs.

Results

mAb1 opalescence and liquid-liquid phase separation are modulated by ionic strength

We started out by investigating the phase behavior of 45 mg/mL mAb1 samples in 10 mM histidine pH 6.5, with increasing NaCl concentration (0-150 mM) at room temperature (RT). Inspection of the solutions revealed an increase in the solution opalescence (Figure 1A) and right-angle light scattering (RALS) intensity (Figure 1B) at low salt, followed by a less steep decrease at higher NaCl concentrations, until returning to a clear solution at 150 mM NaCl. To determine the origin of this high opalescence (which we will simply refer to as opalescence from now on), we next investigated selected mAb solutions by brightfield microscopy, which are highlighted in colors in Figure 1B. Images of the 0 mM and 150 mM NaCl samples with no solution opalescence were clear under the microscope (Figure 1C). However, samples at 10 and 22.5 mM NaCl were characterized by distinct solution morphologies, despite comparably high scattering intensities and similar visual appearance. At 10 mM NaCl, spherical droplets, with liquid-like properties were observed (see Figures 1C and S1), while increasing the NaCl concentration to 22.5 mM abolished this

142 phenomenon. The presence of both opalescence as a single phenomenon (14) or associated with
143 LLPS in a narrow NaCl range complicates the determination of the LLPS regime by e.g. turbidity
144 measurements (16). We therefore combined simultaneous microfluidic mixing and fluorescence
145 detection of LLPS events for the high-throughput mapping of the mAb1 phase diagram at low NaCl
146 concentrations and over a broad mAb1 concentration range (30). Briefly, this method relies on the
147 precise encapsulation of predefined combinations of mAb1, buffer and NaCl solutions into
148 microenvironments surrounded by an oil phase, for which the presence of LLPS is individually
149 assessed via fluorescence detection. As depicted in Figure 1D (and Figure S2-S3), adding as little
150 as 5 mM NaCl induced LLPS of mAb1 at concentrations above an approximate saturation
151 concentration of 30 mg/mL. Remarkably, above 10 mM NaCl, the system exited the de-mixed
152 regime and underwent reentrant phase transition (31, 32) into a homogeneous state, characterized
153 by high light scattering intensities and absence of droplets.

154

155 **Opalescence and LLPS have similar interaction fingerprints**

156 To differentiate between opalescence and LLPS, we studied the protein-protein interactions (PPIs)
157 governing these phenomena, by measuring the small- and wide-angle X-ray scattering (SAXS and
158 WAXS) profiles of our selected formulations at 45 mg/mL. Drastic differences in the scattering
159 intensity I(**q**) were observed in the low **q** region of the scattering curves (larger distances), while
160 the curves overlapped in the high **q** region (Figure 2A). Both the LLPS (10 mM NaCl) and
161 opalescent (22.5 mM NaCl) samples were characterized by highly attractive interactions, as
162 inferred from the upturn of the scattering intensity I(**q**) at low **q**, compared to the form factor (FF)
163 obtained in the absence of PPIs (black in Figure 2A, S4). This feature was, however, more
164 prominent for the LLPS condition. A common strategy to minimize such attractive interactions in
165 mAb formulations relies on the addition of L-arginine HCl (hereafter referred to as arginine) (9, 33).
166 Indeed, adding 150 mM arginine to a formulation in which mAb1 would have otherwise undergone
167 LLPS (i.e. 45 mg/mL mAb1 + 10 mM NaCl in 10 mM histidine, pH 6.5), no LLPS was observed
168 (Figure S5A). This was also the case for the opalescent sample (Figure S5B). When comparing
169 the effect of adding arginine versus 150 mM NaCl, which similarly decreased solution light
170 scattering, the former resulted in a SAXS/WAXS scattering curve overlapping with the FF, while
171 the latter presented a deviation therefrom, indicating residual attractive forces in solution.

172 We next extracted structure factor contributions, S(**q**), from the total scattering intensity, to
173 emphasize the nature of PPIs at our selected conditions (Figure 2B). For both the LLPS (pink) and
174 opalescent (purple) conditions, this analysis revealed a large positive slope in S(**q**) at low **q**.
175 Furthermore, positional correlation peaks were observed at **q**=0.06 $Å^{-1}$ and 0.1-0.12 $Å^{-1}$,
176 corresponding to real space distances of 104 and 52 Å, i.e. the diameter and radius of a mAb (34).
177 Such an S(**q**) profile is reconcilable in terms of the formation of reversible mAb clusters in solution
178 (5, 35). Interestingly, the same peaks were also visible for the condition containing 150 mM arginine
179 (termed 10 mM NaCl+Arg here, grey) and 150 mM NaCl (green) but with decreased peak definition,
180 probably due to the stronger screening of electrostatic interactions at higher ionic strength (IS) (36).

181 To study the progression of PPIs involved in cluster formation and LLPS, we added a temporal
182 dimension to our SAXS experiment, by coupling a microfluidic device to the beamline as described
183 in (37) and illustrated in Figure S6. Under LLPS-inducing conditions for mAb1, the above-
184 mentioned fingerprint for cluster formation was already visible 12 ms after the mixing point and
185 increased slightly until stabilizing after ≈1.5s (Figure 2C, pink). Addition of arginine or 150 mM NaCl
186 conditions gradually decreased these interactions, albeit more slowly in the latter case, despite the
187 lower molecular weight (Mw) of NaCl. In all cases, the scattering curves of the final timepoints in
188 the time-resolved experiment overlapped with the static SAXS data, showing a high level of
189 agreement between the two setups (Figure S7). Altogether, this suggests that both LLPS and
190 opalescence have similar underlying molecular fingerprints, characterized by attractive interactions
191 and cluster formation, which can be inhibited using similar strategies.

mAb1 phase behavior is dictated by electrostatic patch-mediated interactions

To dissect the molecular features driving LLPS at 10 mM, opalescence without phase separation at 22.5 mM and a transparent solution at 150 mM NaCl, we employed Monte Carlo (MC) simulations. We first matched the experimental scattering curves, I(**q**), using a 174-bead coarse-grained model of mAb1. We tuned our model to reproduce the strength of the short-range hydrophobic attractions, (ε_{ij} in equation 2, Materials and Methods), using the I(**q**) curve corresponding to 150 mM NaCl, where we expected hydrophobicity to be the most prominent, due to the electrostatic screening (green in Figure 3A). This could be achieved at ε_{ij}=0.3185 kJ/mol. However, the simulated I(**q**) curves for the 22.5 mM and 10 mM NaCl at pH 6.5 showed a less attractive behavior compared to the SAXS data (Figure 3A). The structures used for the simulations at pH 6.5 are shown in Figure 3B. Their 1 k_BT/e electrostatic surface potentials at 10, 22.5 or 150 mM NaCl show a highly anisotropic charge distribution, and we estimated a high positive net charge of the mAb (Figure S8). Considering the latter and the sole bulk screening effect of NaCl, a high degree of repulsion should be indeed expected at low salt, which is gradually screened at higher salt concentrations. This is also captured by our two-body simulations in terms of calculated mAb reduced second osmotic virial coefficient, B_2^*, from the potential of the mean force (PMF in Figure S9), and the electrostatic multipole expansion (Figure S10). The decreasing B_2^* values obtained at pH 6.5 at increasing NaCl concentrations in Figure 3C originate from a progressively screened repulsion, mirroring the trend observed for the simulated I(**q**) (Figure 3A).

To rationalize the inverse trend observed experimentally, a key aspect needs to be considered. Prominent positive surface patches (blue in Figure 3B) are known to be involved in mAb self-assembly (38–41). In general, electrostatic patches can interact with salt ions and effectively alter the solution pH experienced locally by moving it towards the isoelectric point (pI) (42). Following this rationale, we evaluated the B_2^* at pH values approaching the pI of mAb1. At pH 7.5, B_2* nearly overlaps at all salt conditions, indicating a similar interaction profile (Figure 3C). At the pI (≈8.55), however, the order inverts: the 10 mM salt curve (pink) exhibits the strongest attraction, followed by 22.5 mM (purple), while the highest salt concentration (green) is the least attractive, recapturing the experimental trends. Looking at the multipole decomposition analysis (Figures S10-S12), this trend is explained by a gradual decrease in the repulsive ion-ion interactions from pH 6.5 to 8.55, until vanishing completely and leaving only attractive dipole–dipole contributions. The presence of the mAb dipole moment at pH 8.55 is evident from the electrostatic isopotential surface (Figure 3D), showing a higher symmetry between the positive (blue) and negative (red) potentials that are gradually screened with increasing salt. We then performed many-mAbs simulations using the 174-bead model and calculated the I(**q**) curves at pH 8.55. As shown in Figure 3E, our simulations at pH 8.55 successfully recapitulate the experimental trend, strongly supporting a mechanistic scenario in which salt-induced saturation of the mAb1 electrostatic patch drives a pH shift toward the pI. This shift plays a pivotal role in enhancing the contribution of attractive hydrophobic and dipole–dipole interactions, ultimately promoting LLPS at 10 mM NaCl. Upon further salt addition to 22.5 mM NaCl, the strength of dipole–dipole interactions diminishes due to dipole screening (43) and the dense phase is disrupted, but substantial mAb–mAb attraction is maintained, which manifests macroscopically as opalescence without phase separation. At 150 mM NaCl, extensive dipole screening results in reduced inter-mAb attractions.

LLPS/opalescence and stress-induced aggregation of mAb1 are decoupled

Finally, we investigated the link between LLPS and opalescence in mAb formulations and propensity for stress-induced aggregation. We therefore subjected the same formulations (45 mg/mL mAb1, 10, 22.5, 150 mM NaCl or 10 mM NaCl+Arg) to vigorous stirring (16 hours at 1000 rpm, RT). This resulted in a dramatic turbidity increase in all formulations (Figures 4A and 4B). Interestingly, arginine did not protect against contact stirring despite its reported role as a suppressor of aggregation (44). The visibly aggregated samples were centrifuged for 2 hours at 21.000 *g*, resulting in pellets comparable in size across the different formulations. Strikingly, the 10

242 and 22.5 mM NaCl samples stayed opalescent after stirring. Moreover, the hard centrifugation
243 revealed the presence of a transparent top dilute phase as previously observed for mAb network
244 formation (45). We next verified by brightfield microscopy that aggregates were responsible for the
245 observed pellet (Figure 4C). Interestingly, droplets with preserved liquid-like properties were
246 observed in the soluble fraction of the stirred 10 mM NaCl sample, demonstrating that LLPS
247 persists after harsh stirring or can reform rapidly thereafter (Figure 4C, bottom). Finally, we
248 calculated the monomer recovery in the different formulations. To avoid density gradients from
249 different phases in the LLPS/opalescence samples, we added 150 mM arginine directly to the
250 samples before and after stirring, when measuring their concentrations (Figure 4D). Within the
251 error, no differences in monomer recovery between the samples were detected, suggesting that
252 the stirring-induced aggregation observed is independent of IS (Figure 4E). Aggregation was
253 observed even after the formulations were supplied with 0.15 mg/mL polysorbate 80 (PS80)
254 indicating that the observed phenomena do not solely arise from the air-water interphase but also
255 from the bulk solution (Figure S13).

256 **Discussion**

257 Here, we studied the model antibody mAb1, who undergoes LLPS above a concentration of ~30
258 mg/mL, in a narrow range of low NaCl concentrations in 10 mM histidine buffer at pH 6.5 (Figure
259 1). Above this NaCl range, the mAb1 solution returns to a one-phase state, characterized by a
260 highly opalescent, droplet-free phase, in the vicinity of the upper critical NaCl concentration for
261 LLPS.
262
263 In our SAXS/WAXS studies (Figure 2), we noted a shared interaction fingerprint between LLPS
264 and opalescence, characterized by highly attractive interactions, leading to cluster formation.
265 These were shown to occur within milliseconds upon mixing components, leading to mAb1 LLPS,
266 and could be efficiently mitigated by arginine, resulting in a clear solution (Figure 2 and S5). We
267 observed that addition of 150 mM arginine led to a higher degree of inhibition of these interactions
268 compared to adding 150 mM NaCl. Due to comparable ionic strengths, this indicates that the effect
269 of arginine is not purely ionic, as noted by Tilegenova et al. (46). Notably, the scattering patterns at
270 high **q** values (small distances) overlapped with the form factor both for the LLPS and opalescent
271 conditions, suggesting that these phenomena are not accompanied by large structural
272 rearrangements. Importantly, the macroscopic differences between these two phenomena imply
273 that their molecular underpinnings differ. The sharp response in phase behavior to a slight change
274 in IS as well as the abrogation of LLPS and opalescence further pointed towards key interactions
275 being mainly confined to oppositely charged surface patches (5, 39).
276
277 To clarify this, we performed simulations to reproduce the trends in our experimental X-ray
278 scattering data and obtain a model describing the interactions driving LLPS versus opalescence.
279 The simulations only agreed with the experimental phase behavior when shifting the solution pH
280 towards the pI of mAb1 (see Figure 3A and Figure 3E). This indicates a mechanism in which the
281 highly positive net charge of mAb1 is progressively neutralized while adding salt, leading to an
282 effective shift of the mAb pH towards the pI. Our electrostatic isopotential surface analysis (Figure
283 3B) has shown the presence of a strong positive electrostatic patch ranging from the Fab to Fc
284 domains in mAb1. We hypothesize that in the presence of a small amount of salt (10 mM of NaCl)
285 the electrostatic path gets neutralized, and this causes the pH to shift towards the pI. At the pI, the
286 suppression of the strong ion-ion repulsions allows short-ranged attractive dipole–dipole and
287 hydrophobic interactions to become more prominent, shifting the balance towards a net attraction
288 of mAbs in solution. In this configuration dipole-dipole interactions are strong, as dipoles can align
289 to maximize their interaction energy. This process is at the basis of the formation of stable clusters,
290 leading to droplet formation and LLPS (Figure 3F) (43). The mechanism of the patch neutralization
291 and the consequent shift towards the mAb pI is in line with the work of Pineda et al. (42), who
292 demonstrate that patchy distributions of ionizable groups on protein surfaces significantly affects
293 pH in protein solutions, linking local charge inhomogeneities to deviations between bulk buffer pH

294 and the effective pH experienced by proteins. Similarly, Ausserwöger et al. observed that FUS and
295 PGL3 condensates minimized electrostatic repulsion by buffering towards the pI of the molecules,
296 via the exclusion of buffer molecules (47).
297
298 When a higher amount of salt is added to the solution (22.5 mM of NaCl) the electrostatic patch is
299 neutralized, and the excess ions distribute uniformly over the mAb surface. This causes a partial
300 screening of the dipoles and a consequent misalignment. This translates into weaker dipole-dipole
301 attractions and a consequent incapacity of the system to phase-separate yet preserving some
302 alignment among dipoles and giving rise to the high opalescence (Figure 3F). Clusters responsible
303 for this phenomenon are likely smaller or less stable, compared to those witnessed during LLPS
304 (48). This also explains the small decrease observed in the low-**q** region of the scattering intensity
305 at 22.5 mM NaCl (Figure 2A). At 150 mM NaCl, electrostatic screening becomes much stronger
306 and dipole–dipole interactions are negligible, leaving hydrophobic interactions as main attractive
307 force between mAbs. This makes the solution appear clear as both opalescence and LLPS are
308 disrupted.
309
310
311 Finally, we questioned whether LLPS and opalescence of mAb solutions could lead to increased
312 aggregation (Figure 4). We chose to evaluate this in a forced degradation setup where formulations
313 were subjected to stirring stress, as this has been shown to rapidly induce the formation of large
314 amounts of aggregates for mAbs (49–52). In this setup, stirring of all mAb1 formulations produced
315 solid pellets of comparable sizes, suggesting that its effect is independent of IS in the timeframe
316 studied (Figure 4B). Importantly, LLPS was conserved at 10 mM NaCl, coexisting with solid
317 aggregates (Figure 4C). This was also the case for samples containing PS80, suggesting that the
318 bulk solution also contributes to the overall aggregation (Figure S13). The fact that hard
319 centrifugation couldn't completely sediment LLPS droplets suggests that their volume fraction is
320 small and that there could exist an equilibrium between them and clusters in solution, as shown for
321 other systems (17, 24, 53). Finally, the observation that LLPS and opalescence were unaffected
322 by stirring and that the same amount of mAb material was converted into aggregates in all
323 formulation points towards the presence of two decoupled mechanisms. One in which mAb1 self-
324 association is dependent on IS, leading to charge modulation of the mAb1 surface in such a way
325 that weak attractive interactions can amount to LLPS or opalescence, depending on the level of
326 charge screening. The other stress-induced mechanism is independent of IS (and hence
327 LLPS/opalescence), resulting in the formation of solid aggregates. Hence, mAb1 LLPS and
328 opalescence are not inherently associated with an increased proclivity for aggregation in our
329 accelerated setup. Whether the effects observed under conditions of harsh stirring translate into
330 long-term stability during, for example, storage remains an important question for future
331 investigation. Nevertheless, the observation that LLPS of mAb1 remains unaffected by aggregation
332 following harsh stirring stress suggests that this phenomenon is stable within mAb formulations.
333 This stability could potentially be harnessed to protect mAbs from other manufacturing stresses or
334 to enable formulations at even higher concentrations. More quantitative, experimental studies,
335 combined with simulations (25) may help in uncovering possible liquid-to-solid transitions over
336 longer timescales under these conditions.

337 Taken together, our data highlight the diverse phase behavior of mAb1, characterized by LLPS at
338 low salt, followed by reentrant phase transition to a highly opalescent state, both driven by attractive
339 interactions and cluster formation. To our knowledge, the present study represents one of the very
340 few studies showing that monovalent ions can induce reentrant phase transitions in mAb
341 formulations. We propose that localized interactions between surface patches and solvent ions
342 modulate the effective pH experienced by mAb1 and steer it towards a more charge neutral state,
343 where dipole-dipole and hydrophobic interactions can dominate and induce LLPS or opalescence,
344 depending on the level of dipole screening by NaCl. Finally, LLPS and opalescence have
345 traditionally been viewed as precursors of aggregation in mAb formulations. Here, we report a not

346 so straightforward relation between these phenomena, which should be taken into consideration
347 during the rational design of mAb formulations.
348
349
350 **Materials and Methods**
351
352 **Model antibody**
353 The model mAb used in this work, mAb1, was supplied by Novo Nordisk A/S in a proprietary
354 formulation before being stored at -20°C as aliquots.
355
356 **Buffer and stock preparation**
357
358 A buffer containing 10 mM L-histidine was prepared freshly using reagent grade L-histidine
359 (ReagentPlus®, ≥99% TLC, H8000, Sigma Aldrich) in Milli-Q water and the pH was adjusted to 6.5.
360 Sodium chloride (1.37017.5000, Merck), L-arginine HCl (EMPROVE® EXPERT, Ph. Eur., ChP, JP,
361 USP, 1.01587, Sigma Aldrich) and polysorbate 80 stocks (1.37171, high purity, EMPROVE®
362 EXPERT, Ph. Eur., ChP, JP, NF, Sigma Aldrich) were prepared in buffer and filtered through a 0.1
363 um Whatman Anotop filter (GE Healthcare, Cat no: 6809-2012).(53)
364
365 **Buffer exchange by dialysis**
366
367 Two rounds of dialysis were carried out using Slide-A-Lyzer™ cassettes (A52976, Merck, 20 kDa
368 Mw cutoff) in buffer for two hours at RT (22°C) and one round overnight (16 hours) at 4°C using
369 fresh buffer with a volume 500 times larger than the sample volume at each step.
370
371
372 **Sample concentration determination**
373
374 Protein concentrations were determined as independent duplicates by measuring the UV-Vis
375 absorbance at 280 nm on a NanoDrop™ One C spectrophotometer. Serial 1:1 dilutions of the mAb
376 stock solution in buffer were prepared from a factor of 2 to 64. The absorbance of each dilution was
377 measured using a theoretical molar extinction coefficient at 280 nm and the Mw before being
378 multiplied by the dilution factor.
379
380
381 **Right-angle static light scattering**
382
383 Static light scattering experiments were performed at 90° with a 635 nm semiconductor laser
384 (Labbot spectrophotometer, ProbationLabs, Sweden). Samples were transferred to a high
385 precision quartz glass, 10x4 mm light pathlength cuvette (104F-10-40, Hellma Analytics, Germany).
386 Measurements were performed at RT, on independent duplicate samples. These were filtered
387 through a 0.1 um Whatman Anotop filter (GE Healthcare, Cat no: 6809-2012). As soon as the
388 scattering signal stabilized, ten consecutive measurements were performed before being
389 averaged. The data was normalized to the highest scattering intensity.
390
391 **Brightfield microscopy**
392
393 Brightfield microscopic images were acquired at RT with a Zeiss Axioscope 5 equipped with an
394 Axiocam 305 color camera, through an LD Plan-Neofluar 20x/0.4 objective and processed using
395 ImageJ software (54).
396
397 **Combinatorial microfluidic mixing (PhaseScan)**
398

399 The phase space of mAb1 as a function of NaCl was mapped out at room temperature using
400 combinatorial microfluidic mixing setup, according to published procedures (30, 47). Pre-defined
401 combinations of Alexa647 N-hydroxy succinimidyl ester labeled mAb1, 10 mM histidine buffer (pH
402 6.5) and a 40 mM NaCl stock containing Alexa488 dye were encapsulated in HFE-7500
403 oil (FluoroChem) supplied with 1.2% (w/V) fluorosurfactant, (RAN Biotechnologies) by flowing the
404 latter into the microfluidic device at a constant flowrate. A total of 46581 droplets containing pre-
405 defined combinations of aqueous components were evaluated for the presence of LLPS (Figures
406 S2 and S3) using an inverted fluorescence microscope (OpenFrame, Cairn Research, Faversham,
407 UK) equipped with a camera (Kinetix, Photometrics, Tucson, AZ, USA, 20x objective). The
408 fluorescence intensities in the separate channels were used to back calculate the mAb1 and NaCl
409 concentrations for each droplet. A grid-map visualization was achieved by binning the individual
410 data points as described in (47).
411
412 **Synchrotron size-exclusion chromatography (SEC)-SAXS for form factor determination**

413 SEC–SAXS experiments were performed at the P12 EMBL BioSAXS beamline, at PETRA III,
414 EMBL Hamburg, operated at a fixed energy (10 keV, λ = 0.124 nm). The form factor was
415 determined at room temperature by SEC-SAXS using a Superdex S200 column coupled to an
416 Agilent1260 Infinity Bio-Inert high performance liquid chromatography (HPLC) system with an in-
417 built temperature-controlled auto-sampler. A total volume of 70 µL mAb1 solution at a concentration
418 of 10 mg/mL in 10 mM histidine pH 6.5+150 mM NaCl was injected into the column. The same
419 buffer was used as mobile phase, and the flowrate was set to 0.65 mL/min. SAXS data was
420 collected for the whole column run. The resulting frames were processed using CHROMIXS from
421 the ATSAS package (55). See Figure S4 for the SEC-SAXS chromatogram and resulting form
422 factor data. By fitting the Guinier region (56) of the obtained form factor, we determined the radius
423 of gyration of mAb1 to be 50 Å, as expected for a standard antibody (34).

424 **SAXS/WAXS**

425 SAXS and WAXS data of mAb1 at 45 mg/mL in 10 mM histidine pH 6.5 containing 10, 22.5 and
426 150 mM NaCl or 10 mM NaCl+ 150 mM L-arginine HCl at room temperature was collected at the
427 P12 (PETRA III, DESY synchrotron, Hamburg) and CoSAXS beamlines (MaxIV laboratory, Lund
428 University), following standard procedures. Frames of the measured total scattering intensity I(**q**)
429 as a function of the momentum transfer **q** were averaged and buffer subtracted. The curves were
430 then absolute scaled in ATSAS (57), using water and empty capillary measurements, performed
431 under the same conditions. The structure factor S(**q**) was obtained by dividing the scaled buffer-
432 subtracted scattering curve with the form factor.

433 **Time-resolved solution SAXS**

434 Time-resolved solution SAXS was performed at the CoSAXS beamline at the MAX IV Laboratory,
435 using a microfluidic sample delivery system (35). Briefly, solution stocks (or buffer) are added to
436 the inlets of a microfluidic-chip, with three inlets (cyclo-olefin copolymer COC/TOPAS®, 300x400
437 µm cross-section, Microfluidic ChipShop). These a mixed at a mixing point to reach the condition
438 of interest, after which SAXS is recorded at different locations in the channel.

439 Two inlets contained 60 mg/mL freshly dialyzed mAb stock, while the last inlet in the middle position
440 was supplied with either buffer or excipient stock solutions (NaCl and/or L-Arginine HCl) stocks. At
441 the mixing point, the mAb is diluted by a factor of 2/3 and the excipients, by a factor of 1/3. SAXS
442 data was collected at two of the inlets prior to mixing, the mixing point and 21 positions from the
443 mixing point at a total flowrate of 60 µL/min as the chip was translated along **z**. The time resolution
444 of the experiment was determined by a combination of the flowrate and the distance from the mixing
445 point. SAXS data was recorded with an incident X-ray beam of wavelength $\lambda = 0.99$ Å, with a
446 sample-to-detector (Eiger2 X 4m) distance of 3.5 m yielding a q-range of $0.004 < \mathbf{q} < 0.3$ Å^{-1}. The
447 background of each inlet was measured prior to replacing the contents of the inlet 1 and 3 with

mAb solution. 40 frames were recorded at each point for a total of 50 ms and averaged. The scattering curves were absolute scaled using water and empty capillary measurements performed under the same conditions. All processing was performed using the Primus package in the ATSAS data analysis software (57) and S(**q**) was calculated as described in the previous section.

Structure preparation for Monte Carlo simulations

A structural model of mAb1 was generated by replacing the Fab domains in a public IgG4 crystal structure (PDB:5DK3) with those of mAb1. Using the Visual Molecular Dynamics visualization program (58), the mAb sequence was extrapolated. The conformational energy was minimized using OpenMM (version 8.3) (59), as follows. Missing hydrogen atoms were added to reflect the protonation state at pH 6.5. The system was then parametrized using the Amber14 ff14SB (60) force field for proteins, combined with the TIP3Pwater model (61). The Particle Mesh Ewald method (62)was employed, to deal with long-range electrostatics. Using the Langevin integrator (63) at 300 K, iterative energy minimizations were executed, using OpenMM's L-BFGS optimizer (64), to reduce potential energy by removing steric clashes and relaxing strained geometries. Starting from the high positive potential energy we reached a minimum plateau after performing 1000 steps of maximum 100 iterations.

Coarse-graining and charge calculation

From the atomistic energy-minimized structure of mAb1, a coarse-grained (CG) model at the amino acid (aa) level was generated, by replacing each aa with a single bead, positioned at its center of mass. To each bead was assigned an effective diameter, σ_i according to the equation:

$$\sigma_i = \left(\frac{6M_w}{\pi\rho}\right)^3 \qquad 1$$

where ρ = 1 g/mol is an average aa density (65) and M_w, the mass of the single aa. To accurately assign aa charges under varying solution conditions, constant pH Monte Carlo (MC) simulations were performed, using Faunus (66, 67). To each bead was assigned an intrinsic pK_a value (68) reflecting the acid-base equilibrium constant of the isolated side chain under ideal solvent-exposed conditions (66). These values underpin the protonation/deprotonation equilibria that drive charge fluctuations during the simulation. Within Faunus (version 2.16.3), the protonation states of each titratable bead were treated as stochastic variables subject to MC moves that emulate the reversible acid dissociation reaction. Proton concentration is implicitly modelled through the input proton activity, corresponding to the pH, which modulates the acceptance probabilities of protonation changes, in accordance with the pK_a values and the local electrostatic environment. By iteratively applying titration moves alongside standard configurational MC steps, the system equilibrates to a charge distribution consistent with the imposed pH and IS. After 10.000 MC sweeps, the protonation states reached a steady-state distribution, allowing for an accurate estimation of the net charge and charge heterogeneity of the mAb. The net charge of mAb1 was then calculated as a function of pH and IS (Figure S8).

A second CG, 174-bead model was developed, by grouping every seven aas of the primary sequence, into a single bead, whose individual diameter (σ_i) was determined using equation 1 from the Mwof the seven residues (Figure S14). Each bead was assigned a net charge equal to the average charge of its constituent residues. To assess the validity of this simplified representation, we compared the form factor calculated from the amino acid-level CG model with that of the 174-bead model. As shown in Figure S8, the two models exhibit strong agreement, indicating that the simplified model preserves essential structural features. This reduced model was primarily employed to investigate the collective behavior of mAb1 through large-scale simulations involving multiple mAbs.

Two-mAb simulations

Using the aa representation of mAb1, we performed two-mAb MC simulations to catch the mAb behavior in the dilute a regime. A first mAb was initially placed in the center of a simulation box, while a second was placed 150 Å away along the **z**-axis. The first mAb could only rotate around its center of mass, while the second could further translate along **z** (Figure S15). mAbs were treated as rigid bodies and interacted with each other through a non-bonded bead-bead potential, U_{ij} which accounts for both electrostatic and short-range interactions:

$$\beta U_{ij} = \frac{\lambda_B z_i z_j}{r_{ij}} e^{\frac{-\lambda_D}{r_{ij}}} + 4\beta\varepsilon_{ij}\left[\left(\frac{\sigma_{ij}}{r_{ij}}\right)^{12} - \left(\frac{\sigma_{ij}}{r_{ij}}\right)^{6}\right] \quad 2$$

where $\lambda_B = \beta e^2/4\pi\varepsilon_0\varepsilon_r$ is the Bjerrum length, with ε_0 being the vacuum permittivity, the relative permittivity of water (being the solvent treated implicitly), $\varepsilon_r = 80$, e the electron unit charge, and $\beta = 1/k_B T$ the inverse thermal energy, where k_B is Boltzmann's constant and the temperature T =300 K. z_i and z_j are the charges of the ith and j^{th} bead, and r_{ij} the distance between them. The bead-bead minimal approach distance, σ_{ij} ,was obtained from equation 1 as $\sigma_{ij} = (\sigma_i + \sigma_j)/2$, while the energy depth of the Lennard Jones interactions, ε_{ij}, was fixed to 0.15 kJ/mol to reproduce a mild attraction. The values for $\sigma_{ij}$are reported in Table S1. The Debye length, λ_D, which accounts for salt screening effect (treated implicitly), is calculated through the relation:

$$\frac{1}{{\lambda_D}^2} = 4\pi\lambda_B\left[Z_{mAb}\rho_{mAb} + 2\rho_{salt} + 2\rho_{buffer}\right] \quad 3$$

where ρ_{mAb} is the mAb number density (which is zero for two-mAb simulations as we are assuming infinite dilution), Z_{mAb} is the net charge, and ρ_{salt} and ρ_{buffer} are, the number densities of salt and of the dissociated buffer ions. Using the simulation setup shown in Figure S15, the radial distribution function of mAb1, g(r), was sampled, from which, the potential of the mean force (PMF), $W(r)$, can be calculated:

$$W(r) = -k_B T \ln g(r) \quad 4$$

The PMF was used to calculate the reduced second osmotic virial coefficient B_2^*, which is defined as:

$$B_2^* = \frac{B_2 - B_2^{hs}}{B_2^{hs}} \quad 5$$

where: $B_2 = B_2^{hs} + B_2^{int} = \frac{2\pi\sigma^3}{3} - 2\pi\int_\sigma^\infty\left[e^{-\beta W(r)} - 1\right]z^2 dz$ (69). B_2^{hs} represents the hard-sphere contribution to the B2 that arises from steric repulsion after approximating the mAb with a sphere of radius equal to the mAb radius of gyration. B_2^{int} is the contribution due to the effective interactions between the mAbs.

With two-mAb simulations, mAb-mAb electrostatic interactions were further characterized. The exact electrostatic energy between two mAbs is the sum of the pairwise Coulomb interactions between all charged beads:

$$U_{exact} = \sum_i \sum_j \frac{q_i q_j}{4\pi\varepsilon_0 |r_{ij}|} \quad 6$$

where r_{ij} is the separation vector between beads *i* and *j,* belonging to the two mAbs. U_{exact} can be approximated by the sum of multipole moments. More specifically, it can be written as a sum of ion-ion, ion-dipole, dipole-dipole, ion-quadrupole, and higher order terms:

$$U_{exact} \approx U_{ion-ion} + U_{ion-dipole} + U_{dipole-dipole} + U_{ion-quadrupole} + \cdots$$

$$= \frac{1}{4\pi\epsilon_0}\left[\frac{q_a q_b}{R} + \frac{q_a(\boldsymbol{\mu}_b \cdot \boldsymbol{R})q_b(\boldsymbol{\mu}_a \cdot \boldsymbol{R})}{R^3} + \frac{\boldsymbol{\mu}_a \cdot \boldsymbol{\mu}_b - 3\frac{(\mu_a \cdot R)(\mu_b \cdot R)}{R^2}}{R^3} + \frac{1}{2}\frac{q_a \boldsymbol{R}^T \boldsymbol{Q}_b \boldsymbol{R} + q_b \boldsymbol{R}^T \boldsymbol{Q}_a \boldsymbol{R}}{R^5} + \cdots\right] \quad 7$$

where q_a/q_b, $\boldsymbol{\mu}_a/\boldsymbol{\mu}_b$and $\boldsymbol{Q}_b/\boldsymbol{Q}_a$ are net charges, dipole, moments and quadrupole moment tensors of the first and second mAb (a and b) and $\boldsymbol{R}$ is the vector connecting their centers of mass.

Many-mAb simulations

Using the 174-bead model, MC simulations of many mAbs were performed, to reproduce the SAXS scattering intensity of high concentration samples. We used 100 rotating and translating mAbs moving inside a cubic box, whose size was chosen to reproduce a given mAb concentration (Figure S16). In this setup, mAbs still interacted with each other through the bead-bead potential from equation 2.

The intensity at a given scattering vector **q** is then computed according to:

$$I(q) = \frac{1}{N_{tot}}\left\langle\left(\sum_i^{N_{tot}} \sin(\boldsymbol{q}\boldsymbol{r_i})\right)^2 + \left(\sum_i^{N_{tot}} \cos(\boldsymbol{q}\boldsymbol{r_j})\right)^2\right\rangle \quad 8$$

where N_{tot} is the total number of scatterers in the system, defined as the product of the number of mAbs and the number of beads per mAb, and $\boldsymbol{r_i}$ and $\boldsymbol{r_j}$ identify the position of the ith and j^{th} bead. The average is performed over a set of scattering vectors, systematically generated by permuting the crystallographic index of the cubic box [100], [110], [111], to define the scattering vector $\boldsymbol{q} = 2\pi p/L(h,k,l)$, where $p = 1,2,\ldots,p_{max}$, and $p_{max} = 25$.

Stirring stress protocol

Selected mAb formulations were prepared as 1 mL solutions of 45 mg/mL mAb1 and filtered through a 0.1 µm Whatman Anotop filter (GE Healthcare, Cat no: 6809-2012). The samples were then divided in two 500 µL aliquots and added to separate 4 mL glass screw vials (45X15 mm, MD Scientific, VF013-1545) with a 5x2 mm cylindrical PFTE-coated stirring bar (BOLA, C 350-03). The vials were capped (Thermo Scientific, B7815-13) and sealed before being placed vertically on a magnetic stirring plate (IKA RO 15) and stirred at 1000 rpm overnight (16h). Aliquots of the samples before stirring were diluted 10 times in 150 mM L-arginine HCl in 10 mM histidine pH 6.5 and their concentration measured.

Monomer recovery after stirring

After stirring, L-arginine HCl in 10 mM histidine pH 6.5 was added directly to the vials at a final concentration of 150 mM. The vials were gently swirled and 400 µL were transferred to microcentrifuge tubes before 2 hours centrifugation at approximately 21000 *g*. Aliquots of the

sample supernatants after stirring and centrifugation were diluted 10 times in 150 mM L-arginine HCl in 10 mM histidine pH 6.5 and their concentration measured, before being divided by the initial sample concentration (see previous section) to obtain what we called the monomer recovery here.

Acknowledgments

The authors acknowledge Novo Nordisk A/S for project funding and providing mAb material. Tobias Palle Holm from the R&ED department at Novo Nordisk A/S is thanked for granting access to the microscope used in this study. The authors also thank Gaetano Invernizzi for mediating the collaboration with the University of Cambridge and general input. Tomas Sneideris is thanked for helping with the analysis of PhaseScan data. Christian Buch Parsbæk is also thanked for his comments to the experiments and research paper. V.F. I.B. S.L. and M.P. acknowledge the support from the VILLUM FONDEN by the Villum Young Investigator Grants “Protein superstructure as Smart Biomaterials (ProSmart)” 2018-2023 (project number: 19175) and “Protein Phase Separation and Solid Transition in Synthetic Cells (ProSeC) 2024-2027 (project number: 53132). V.F. I.B. and S.L. also acknowledge the Novo Nordisk Foundation (projects NNF20OC0065260 and NNF22OC0080141) for financial support. The authors acknowledge the use of the MAX IV Laboratory for time on the CoSAXS beamline under proposal number 20231488. Research conducted at MAX IV, a Swedish national user facility, was supported by the Swedish Research council under contract 20188-07152, the Swedish Governmental Agency for Innovation Systems under contract 2018-04969 and Formas under contract 2019-02496. The authors further acknowledge DESY research center (Hamburg, Germany), for the provision of experimental facilities and time at PETRA III using beamline P22 (proposals 1188 and 1279).

References

1. O. Leavy, Therapeutic antibodies: past, present and future. *Nat Rev Immunol* **10**, 297–297 (2010).

2. K. H. Liu, The history of monoclonal antibody development - Progress, remaining challenges and future innovations. *Ann Med Surg.* **3**, 113–116 (2014).

3. A. Mullard, FDA approves 100th monoclonal antibody product. *Nat Rev Drug Discov* **20**, 491–495 (2021).

4. S. Crescioli, *et al.*, Antibodies to watch in 2024. *MAbs* **16**, 1-35 (2024).

5. N. Skar-Gislinge, F. Camerin, A. Stradner, E. Zaccarelli, P. Schurtenberger, Using Cluster Theory to Calculate the Experimental Structure Factors of Antibody Solutions. *Mol Pharm* **20**, 2738–2753 (2023).

6. J. S. Kingsbury, *et al.*, A single molecular descriptor to predict solution behavior of therapeutic antibodies. *Sci Adv* **6**, 1-11 (2020).

7. P. G. Desai, *et al.*, An Intercompany Perspective on Practical Experiences of Predicting, Optimizing and Analyzing High Concentration Biologic Therapeutic Formulations. *J Pharm Sci* **112**, 359–369 (2023).

607 8. C. Narasimhan, H. Mach, M. Shameem, High-dose Monoclonal Antibodies Via the
608 Subcutaneous Route: Challenges and Technical solutions, an Industry Perspective.
609 *Ther Deliv* **3**, 889–900 (2012).

610 9. R. G. Strickley, W. J. Lambert, A review of Formulations of Commercially Available
611 Antibodies. *J Pharm Sci* **110**, 2590-2608 (2021).

612 10. J. Liu, M. D. H. Nguyen, J. D. Andya, S. J. Shire, Reversible Self-Association
613 Increases the Viscosity of a Concentrated Monoclonal Antibody in Aqueous Solution.
614 *J Pharm Sci* **94**, 1928–1940 (2005).

615 11. A. S. Raut, D. S. Kalonia, Pharmaceutical Perspective on Opalescence and Liquid–
616 Liquid Phase Separation in Protein Solutions. *Mol Pharm* **13**, 1431–1444 (2016).

617 12. H. Nishi, *et al.*, Phase Separation of an IgG1 Antibody Solution under a Low Ionic
618 Strength Condition. *Pharm Res* **27**, 1348–1360 (2010).

619 13. J. Kotarek, *et al.*, Subvisible Particle Content, Formulation, and Dose of an
620 Erythropoietin Peptide Mimetic Product Are Associated With Severe Adverse
621 Postmarketing Events. *J Pharm Sci* **105**, 1023–1027 (2016).

622 14. M. Sukumar, B. L. Doyle, J. L. Combs, A. H. Pekar, Opalescent Appearance of an
623 IgG1 Antibody at High Concentrations and Its Relationship to Noncovalent
624 Association. *Pharm Res* **21**, 1087–1093 (2004).

625 15. E. S. R. Gopal, Critical opalescence. *Resonance* **5**, 37–45 (2000).

626 16. S. Alberti, A. Gladfelter, T. Mittag, Considerations and Challenges in Studying Liquid-
627 Liquid Phase Separation and Biomolecular Condensates. *Cell* **176**, 419–434 (2019).

628 17. S. Alberti, *et al.*, Current practices in the study of biomolecular condensates: a
629 community comment. *Nat Commun* **16**, 1-14 (2025).

630 18. S. Alberti, *et al.*, A User's Guide for Phase Separation Assays with Purified Proteins. *J*
631 *Mol Biol* **430**, 4806–4820 (2018).

632 19. S. Wegmann, *et al.*, Tau protein liquid–liquid phase separation can initiate tau
633 aggregation. *EMBO J* **37**, 1-21 (2018).

634 20. M. Fukuyama, *et al.*, Detection of Fibril Nucleation in Micrometer-Sized Protein
635 Condensates and Suppression of Sup35NM Fibril Nucleation by Liquid–Liquid Phase
636 Separation. *Anal Chem* **95**, 9855–9862 (2023).

637 21. Y. Shen, *et al.*, The liquid-to-solid transition of FUS is promoted by the condensate
638 surface. *Proceedings of the National Academy of Sciences* **120** (2023).

639 22. M. Linsenmeier, *et al.*, The interface of condensates of the hnRNPA1 low-complexity
640 domain promotes formation of amyloid fibrils. *Nat Chem* **15**, 1340–1349 (2023).

641 23. B. Das, *et al.*, A Zn-dependent structural transition of SOD1 modulates its ability to
642 undergo phase separation. *EMBO J* **42** (2023).

643 24. S. Ray, *et al.*, Mass photometric detection and quantification of nanoscale α-synuclein
644 phase separation. *Nat Chem* **15**, 1306–1316 (2023).

645 25. B. Szała-Mendyk, T. M. Phan, P. Mohanty, J. Mittal, Challenges in studying the liquid-
646 to-solid phase transitions of proteins using computer simulations. *Curr Opin Chem*
647 *Biol* **75**, 1-11 (2023).

648 26. A. M. Küffner, *et al.*, Sequestration within biomolecular condensates inhibits Aβ-42
649 amyloid formation. *Chem Sci* **12**, 4373–4382 (2021).

650 27. T. Das, *et al.*, Tunable metastability of condensates reconciles their dual roles in
651 amyloid fibril formation. *Mol Cell* **85**, 2230-2245 (2025)

652 28. E. Pantuso, *et al.*, On the Aggregation and Nucleation Mechanism of the Monoclonal
653 Antibody Anti-CD20 Near Liquid-Liquid Phase Separation (LLPS). *Sci Rep* **10**, 8902
654 (2020).

655 29. J. E. Bramham, S. A. Davies, A. Podmore, A. P. Golovanov, Stability of a high-
656 concentration monoclonal antibody solution produced by liquid–liquid phase
657 separation. *MAbs* **13** (2021).

658 30. W. E. Arter, *et al.*, Biomolecular condensate phase diagrams with a combinatorial
659 microdroplet platform. *Nat Commun* **13**, 1-10 (2022).

660 31. G. L. Dignon, W. Zheng, Y. C. Kim, J. Mittal, Temperature-Controlled Liquid–Liquid
661 Phase Separation of Disordered Proteins. *ACS Cent Sci* **5**, 821–830 (2019).

662 32. G. Krainer, *et al.*, Reentrant liquid condensate phase of proteins is stabilized by
663 hydrophobic and non-ionic interactions. *Nat Commun* **12**, 1085 (2021).

664 33. S. Oki, S. Nishinami, Y. Nakauchi, T. Ogura, K. Shiraki, Arginine and its Derivatives
665 Suppress the Opalescence of an Antibody Solution. *J Pharm Sci* **111**, 1126–1132
666 (2022).

667 34. S. Saurabh, *et al.*, Understanding the Stabilizing Effect of Histidine on mAb
668 Aggregation: A Molecular Dynamics Study. *Mol Pharm* **19**, 3288–3303 (2022).

669 35. A. A. Chowdhury, *et al.*, Characterizing Protein–Protein Interactions and Viscosity of a
670 Monoclonal Antibody from Low to High Concentration Using Small-Angle X-ray
671 Scattering and Molecular Dynamics Simulations. *Mol Pharm* **20**, 5563–5578 (2023).

672 36. A. Gulotta, *et al.*, Combining Scattering Experiments and Colloid Theory to
673 Characterize Charge Effects in Concentrated Antibody Solutions. *Mol Pharm* **21**,
674 2250–2271 (2024).

675 37. F. Herranz-Trillo, *et al.*, Time-resolved scattering methods for biological samples at
676 the CoSAXS beamline, MAX IV Laboratory. *Methods Enzymol* **709,** 245–296 (2024).

677 38. H. Ausserwöger, *et al.*, Surface patches induce nonspecific binding and phase
678 separation of antibodies. *Proc Natl Acad Sci USA.* **120** (2023).

679 39. W. Li, *et al.*, Charge-Induced Patchy Attractions between Proteins. *J Phys Chem B*
680 **119**, 503–508 (2015).

681 40. T. Matsuoka, R. Miyauchi, N. Nagaoka, J. Hasegawa, Mitigation of liquid–liquid phase
682 separation of a monoclonal antibody by mutations of negative charges on the Fab
683 surface. *PLoS One* **15**, e0240673 (2020).

684 41. S. Yadav, T. M. Laue, D. S. Kalonia, S. N. Singh, S. J. Shire, The Influence of Charge
685 Distribution on Self-Association and Viscosity Behavior of Monoclonal Antibody
686 Solutions. *Mol Pharm* **9**, 791–802 (2012).

687 42. S. P. Pineda, P. M. Blanco, R. Staňo, P. Košovan, Patchy Charge Distribution Affects
688 the pH in Protein Solutions during Dialysis. *Langmuir* **41**, 5387–5398 (2025).

689 43. S. N. Singh, S. Yadav, S. J. Shire, D. S. Kalonia, Dipole-Dipole Interaction in Antibody
690 Solutions: Correlation with Viscosity Behavior at High Concentration. *Pharm Res* **31**,
691 2549–2558 (2014).

692 44. S. Ren, Effects of arginine in therapeutic protein formulations: a decade review and
693 perspectives. *Antib Ther* **6**, 265–276 (2023).

694 45. Y. Nakauchi, *et al.*, Opalescence Arising from Network Assembly in Antibody Solution.
695 *Mol Pharm* **19**, 1160–1167 (2022).

696 46. C. Tilegenova, *et al.*, Dissecting the molecular basis of high viscosity of monospecific
697 and bispecific IgG antibodies. *MAbs* **12,** e1692764-1-e1692764-11 (2020).

698 47. H. Ausserwöger, *et al.*, Biomolecular condensates sustain pH gradients at equilibrium
699 through charge neutralisation. bioRxiv [Preprint] (2024).
700 https://doi.org/10.1101/2024.05.23.595321 785 (accessed 30 October 2025).

701 48. W. D. Kimball, *et al.*, Growth of Clusters toward Liquid–Liquid Phase Separation of
702 Monoclonal Antibodies as Characterized by Small-Angle X-ray Scattering and
703 Molecular Dynamics Simulation. *J Phys Chem B* **129**, 2856–2871 (2025).

704 49. T. Ishikawa, N. Kobayashi, C. Osawa, E. Sawa, K. Wakamatsu, Prevention of Stirring-
705 Induced Microparticle Formation in Monoclonal Antibody Solutions. *Biol Pharm Bull*
706 **33**, 1043–1046 (2010).

707 50. S. N. Telikepalli, *et al.*, Structural Characterization of IgG1 mAb Aggregates and
708 Particles Generated Under Various Stress Conditions. *J Pharm Sci* **103**, 796–809
709 (2014).

710 51. A. S. Sediq, R. B. van Duijvenvoorde, W. Jiskoot, M. R. Nejadnik, No Touching!
711 Abrasion of Adsorbed Protein Is the Root Cause of Subvisible Particle Formation
712 During Stirring. *J Pharm Sci* **105**, 519–529 (2016).

713 52. S. Telikepalli, *et al.*, Physical Characterization and In Vitro Biological Impact of Highly
714 Aggregated Antibodies Separated into Size-Enriched Populations by Fluorescence-
715 Activated Cell Sorting. *J Pharm Sci* **104**, 1575–1591 (2015).

716 53. M. Kar, *et al.*, Solutes unmask differences in clustering versus phase separation of
717 FET proteins. *Nat Commun* **15**, 1-21 (2024).

718 54. C. A. Schneider, W. S. Rasband, K. W. Eliceiri, NIH Image to ImageJ: 25 years of
719 image analysis. *Nat Methods* **9**, 671–675 (2012).

720 55. A. Panjkovich, D. I. Svergun, CHROMIXS: automatic and interactive analysis of
721 chromatography-coupled small-angle X-ray scattering data. *Bioinformatics* **34**, 1944–
722 1946 (2018).

56. A. Guinier, G. Fourmet, *Small-Angle Scattering of X-rays* (New York: John Willey and Sons, 1955).

57. K. Manalastas-Cantos, *et al.*, *ATSAS 3.0* : expanded functionality and new tools for small-angle scattering data analysis. *J Appl Crystallogr* **54**, 343–355 (2021).

58. W. Humphrey, A. Dalke, K. Schulten, VMD: Visual molecular dynamics. *J Mol Graph* **14**, 33–38 (1996).

59. P. Eastman, *et al.*, OpenMM 8: Molecular Dynamics Simulation with Machine Learning Potentials. *J Phys Chem B* **128**, 109–116 (2024).

60. J. A. Maier, *et al.*, ff14SB: Improving the Accuracy of Protein Side Chain and Backbone Parameters from ff99SB. *J Chem Theory Comput* **11**, 3696–3713 (2015).

61. L.-P. Wang, T. J. Martinez, V. S. Pande, Building Force Fields: An Automatic, Systematic, and Reproducible Approach. *J Phys Chem Lett* **5**, 1885–1891 (2014).

62. T. Darden, D. York, L. Pedersen, Particle mesh Ewald: An $N \cdot \log(N)$ method for Ewald sums in large systems. *J Chem Phys* **98**, 10089–10092 (1993).

63. G. Bussi, M. Parrinello, Accurate sampling using Langevin dynamics. *Phys Rev E* **75**, 056707-1-056707-7 (2007).

64. Y. Fei, G. Rong, B. Wang, W. Wang, Parallel L-BFGS-B algorithm on GPU. *Comput Graph* **40**, 1–9 (2014).

65. S. Kaieda, M. Lund, T. S. Plivelic, B. Halle, Weak Self-Interactions of Globular Proteins Studied by Small-Angle X-ray Scattering and Structure-Based Modeling. *J Phys Chem B* **118**, 10111–10119 (2014).

66. B. Stenqvist, A. Thuresson, A. Kurut, R. Vácha, M. Lund, *Faunus* – a flexible framework for Monte Carlo simulation. *Mol Simul* **39**, 1233–1239 (2013).

67. M. Lund, M. Trulsson, B. Persson, Faunus: An object oriented framework for molecular simulation. *Source Code Biol Med* **3**, 1-8 (2008).

68. R. L. Thurlkill, G. R. Grimsley, J. M. Scholtz, C. N. Pace, pK values of the ionizable groups of proteins. *Protein Science* **15**, 1214–1218 (2006).

69. S. Mahapatra, *et al.*, Self-Interactions of Two Monoclonal Antibodies: Small-Angle X-ray Scattering, Light Scattering, and Coarse-Grained Modeling. *Mol Pharm* **19**, 508–519 (2022).

757 **Figures**
758

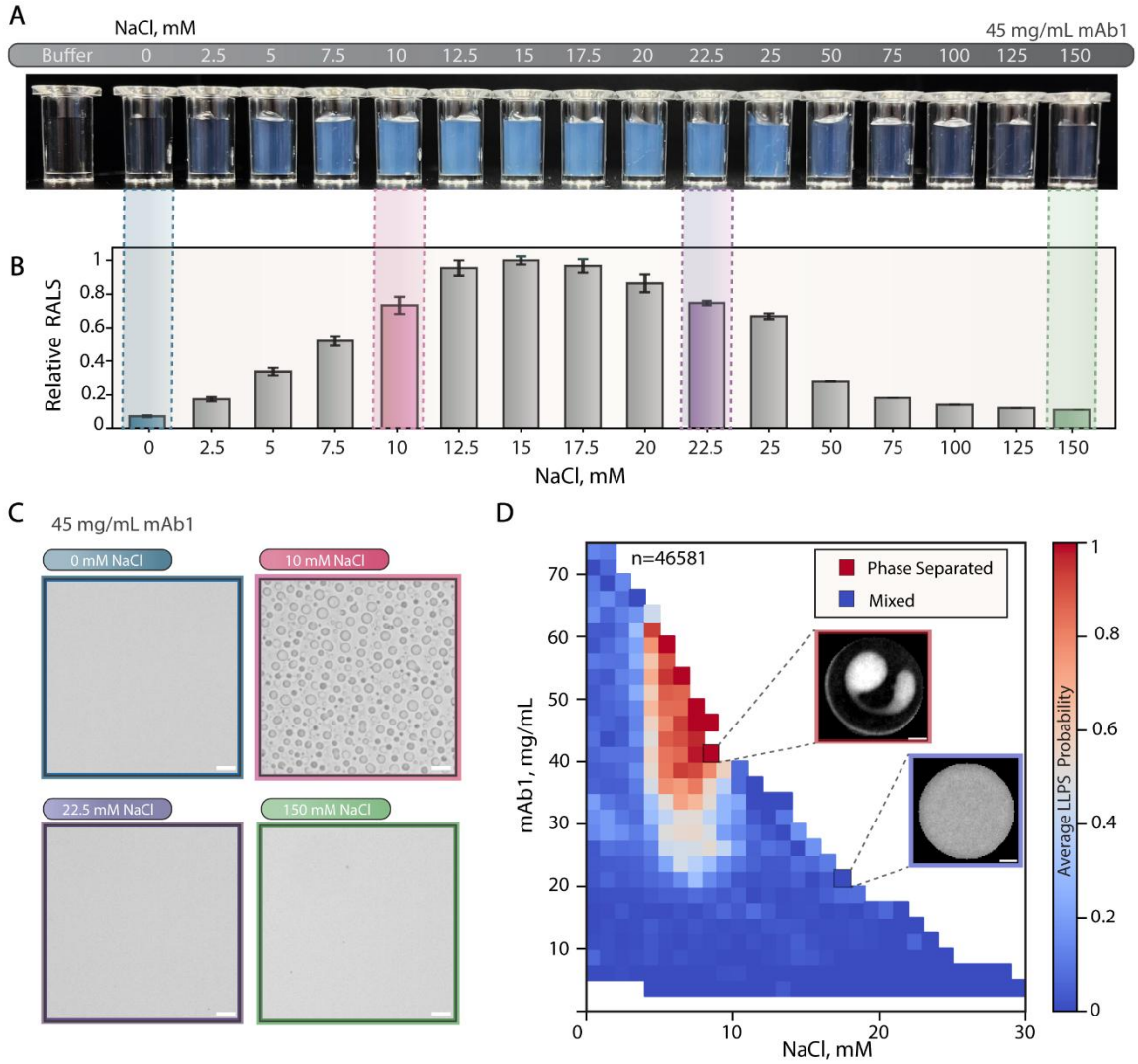

759

760 **Figure 1. Phase behavior of mAb1** (A) Visual appearance and (B) normalized right-angle
761 scattering intensities at 635 nm of 45 mg/mL mAb1 solutions as a function of NaCl, where selected
762 conditions are highlighted in colors. The experiments were independently performed n=2 times and
763 errors represent standard deviations. (C) Brightfield microscopy images of selected conditions (0,
764 10, 22.5 and 150 mM NaCl, 20 µm scalebar). (D) Phase diagram of mAb1 versus NaCl
765 concentration obtained by measuring 46581 independent data points with a combinatorial
766 microfluidic platform (70) (LLPS probability = 1: red, 0.5: white, 0: blue). Representative microscopy
767 images of phase-separated (red)and mixed (no LLPS, blue) are included as insets.

768

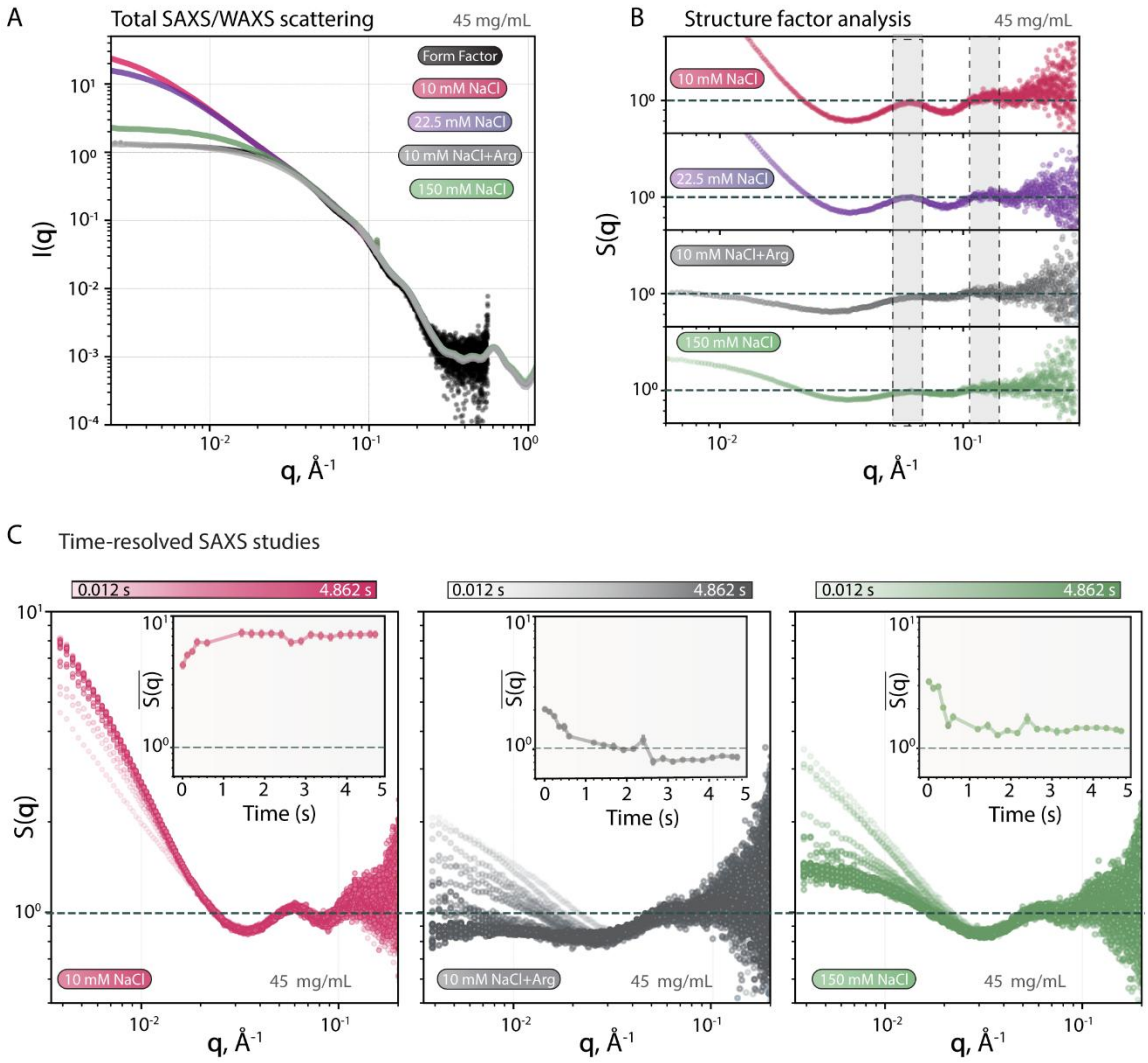

Figure 2: Characterization of interactions underlying mAb1 LLPS and opalescence with SAXS (A) SAXS/WAXS intensities of 45 mg/mL mAb1 + 10 (pink), 22.5 (purple) or 150 mM NaCl (green) and 10 mM NaCl + 150 L-arginine HCl (grey, called 10 mM NaCl+Arg here) as well as the form factor obtained from SEC-SAXS (black) (B) Structure factors measured for the same samples (C) Time-resolved SAXS data (21 datapoints spanning 0.012- 4.862s) of 45 mg/mL+ 10 mM NaCl (pink), 10 mM NaCl+arg (grey) and 150 mM NaCl (green). Averages of the first three S(**q**) values for each curve as a function of time from mixing are included as insets for a clearer overview of the evolution of PPIs.

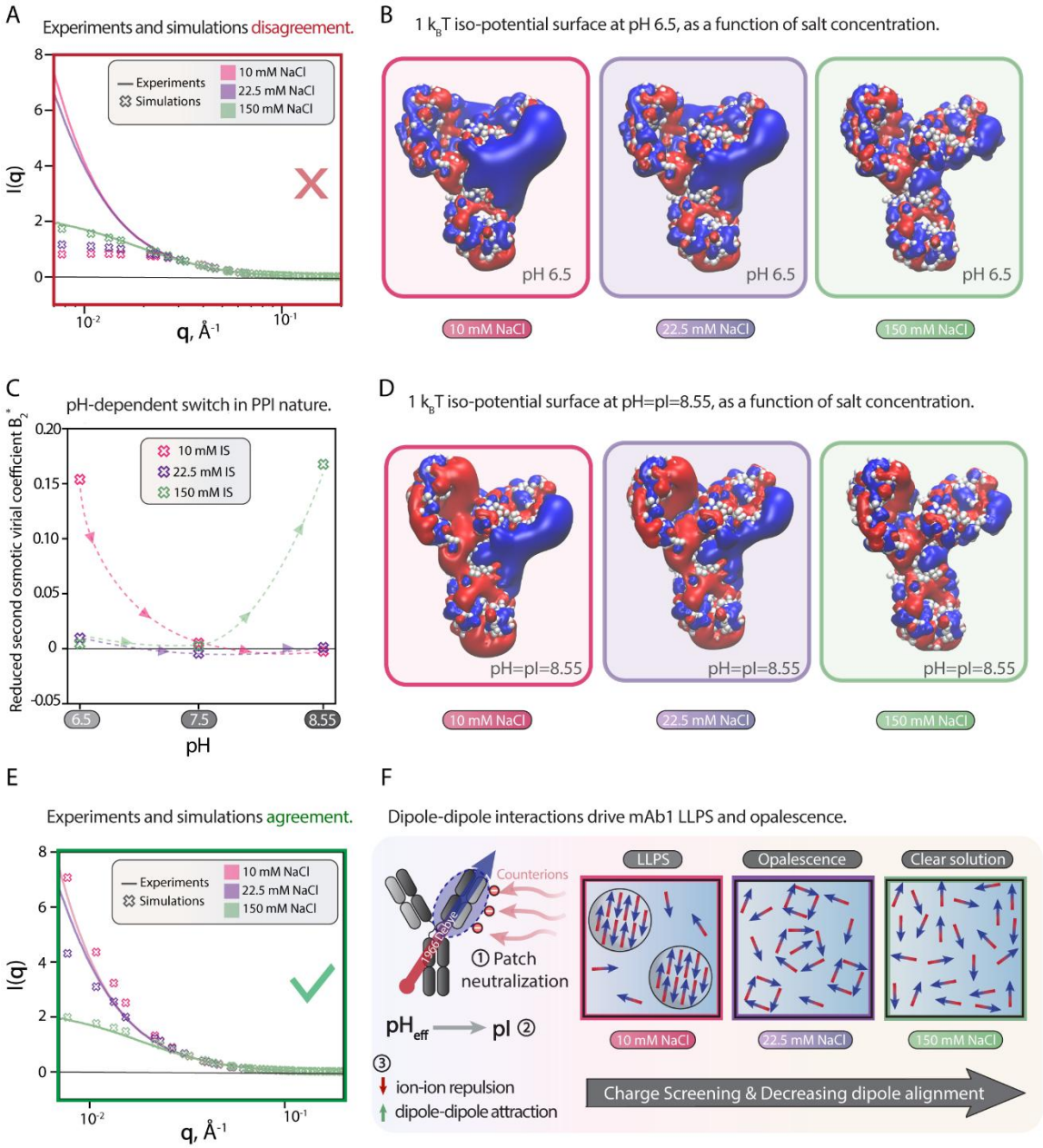

Figure 3: Monte Carlo simulation of mAb1. (A) SAXS intensities, of a 45 mg/mL mAb solution at pH 6.5 obtained from experiments (full lines), and simulations (small *x* symbols) of 100 mAbs coarse-grained with the 174-bead model for different IS (B) Reduced osmotic second virial coefficient, B_2*, of mAb1 obtained from two-mAb simulations at different pH and IS. 1 k_BT/e electrostatic surface potential of mAb1 at (C) pH 6.5 and (D) pH 8.55 for three different IS: 10, 22.5 and 150 mM (left to right) obtained with adaptive Poisson-Boltzmann solver (APBS). Blue indicates a positive electrostatic surface, while red indicates a negative electrostatic surface. The dipole moment of mAb1 was calculated to be 1966.64 Debye at 10 mM NaCl, pH 6.5. (E) Same as (A) but at pH=8.55=pI. (F) Summarizing illustration of molecular mechanism leading to different phenomena based on charge screening effects after the pH shift. At 10 mM NaCl (pH 6.5) interactions are repulsive due to the high net charge of mAb1. As a lot of this excess positive charge is accumulated in a patch in one of its Fab domains, a small addition of NaCl screens this patch to

794 an extent where the overall charge state of mAb1 is neutralized, akin to what it would be close to
795 its pI. Therefore, solution counterions can modulate the local pH experienced by proteins. This
796 suppression of ion-ion repulsion allows mAb1 dipoles to align in a configuration favorable for LLPS.
797 Further charge screening suppresses LLPS at 22.5 mM NaCl but preserves some level of dipole
798 alignment. While the properties of the resulting clusters do not allow them to phase-separate, they
799 nonetheless result in a high level of solution opalescence. Moving even further away from the phase
800 boundary by adding 150 mM NaCl results in an even lower probability of mAb1 dipole aligning,
801 which is witnessed as a clear solution characterized by more repulsive interactions.

802

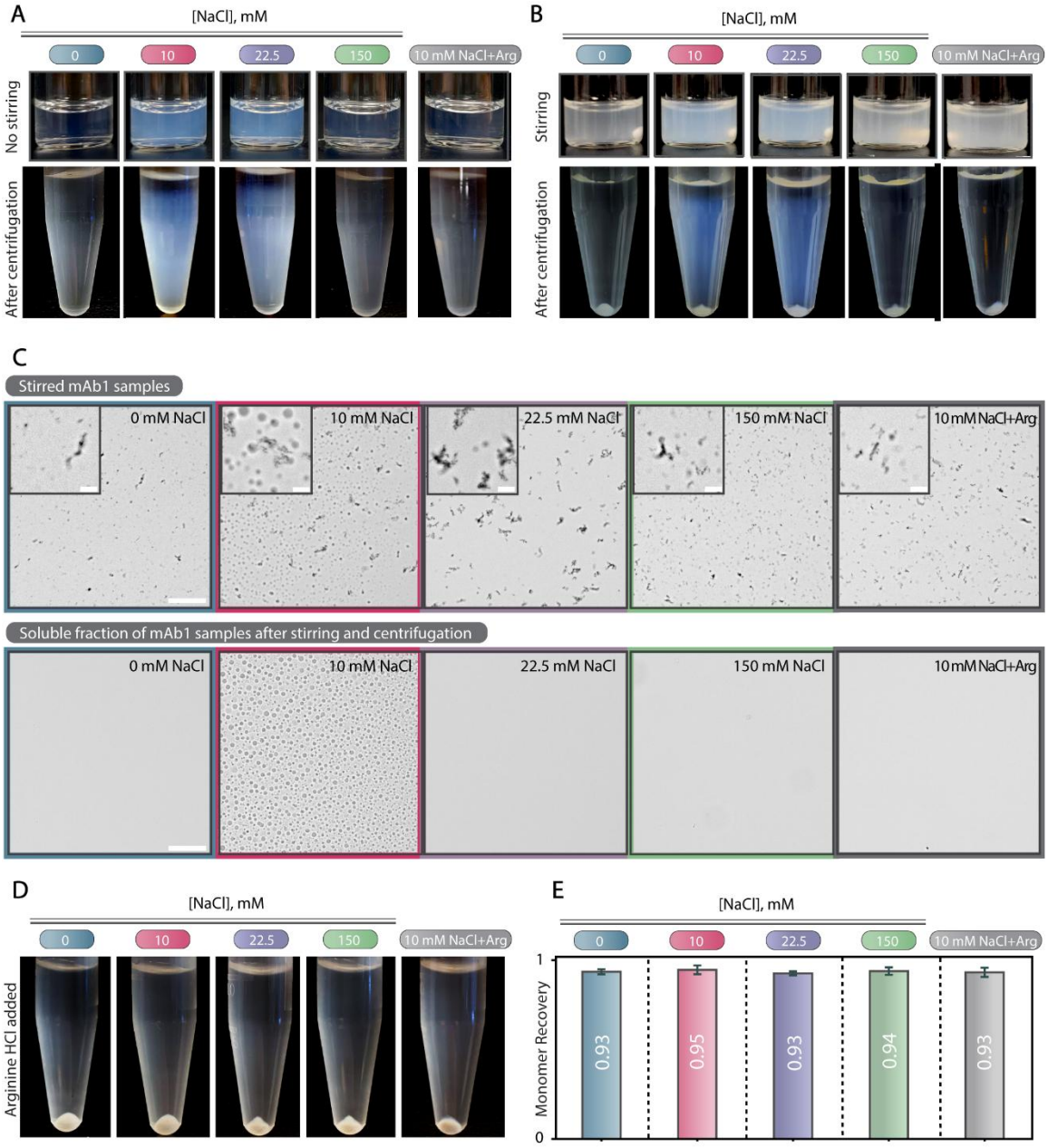

Figure 4. Physical (in)stability of mAb1 samples as a result of stirring stress. Visual appearance of 45 mg/mL mAb1 solutions at pH 6.5 containing 0, 10, 22.5, 150 mM NaCl or 10 mM NaCl+Arg before (A) and after (B) magnetic stirring (16 hours) at 1000 rpm and subsequent centrifugation. (C) Brightfield microscopy of the stirred samples and the supernatant after centrifugation (50 µm scalebar). (D) Representative images of the stirred and centrifuged samples with added L-arginine HCl. Samples were prepared at a larger volume for the images for increased clarity. (E) Monomer recovery of the different conditions measured on two independent samples. The numbers on the individual bars represent the calculated monomer recovery, where 1 and 0 stand for complete and no monomer recovery, respectively. Errors represent standard deviations from duplicate measurements.

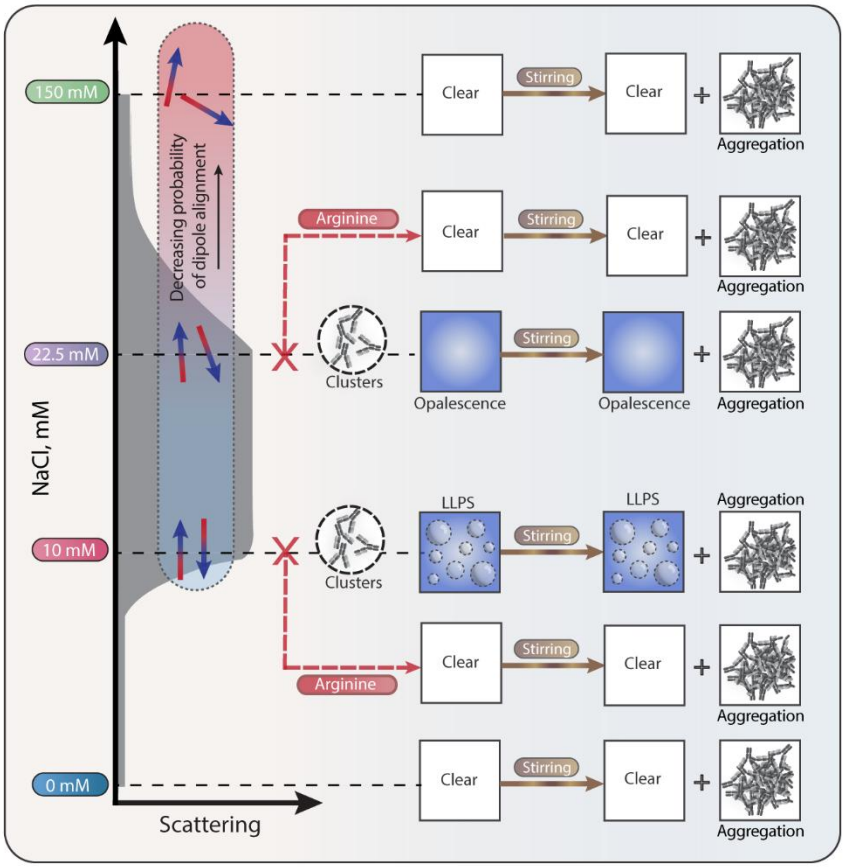

Figure 5: Summary of mAb self-assembly behavior at 45 mg/mL, as a function of NaCl concentration and applied stirring stress. mAb1 LLPS and opalescence occur in a narrow NaCl range can both give rise to similar light scattering intensities, despite having different underlying assembly levels. Both phenomena are characterized by attractive interactions, leading to cluster formation, which can be suppressed by arginine. The level of charge screening in solution dictates the probability of mAb1 dipoles to align favorably and results in large scale association, which decreases with NaCl concentration. Solid aggregation is decoupled from LLPS and opalescence. LLPS and opalescence are unaffected by stirring induced stress.

Supporting Information for

Dissecting the molecular origins of opalescence and phase separation in mAb formulations and their relation to aggregation

Inna Brakti[a,b,1], Samuel Lenton[a,1], Marco Polimeni [a,1], Hannes Ausserwöger[c], Rob Scrutton[c], Anette Henriksen[d], Nikolai Lorenzen[d], Martin Nors Pedersen[b], Jesper Søndergaard Marino[d], Fátima Herranz-Trillo[e], Ann E. Terry[e], Tuomas P. J. Knowles[c], Minna Groenning[b], Vito Foderà[a,*]

[a]Department of Pharmacy, University of Copenhagen, Copenhagen, Denmark 2100, [b]Biophysical Analysis, CMC Analytical Support, Novo Nordisk A/S, Måløv, Denmark 2760, [c]Yusuf Hamied Department of Chemistry, Centre for Misfolding Diseases, University of Cambridge, Cambridge, United Kingdom CB2 1EW, [d] Novo Nordisk A/S, Therapeutics Discovery, Novo Nordisk Park, Måløv 2760, Denmark, [e]MAX IV Laboratory, Lund University, Fotongatan 2, 224 84 Lund, Sweden

* Vito Foderà

Address: Department of Pharmacy, University of Copenhagen, Copenhagen, Denmark 2100

Phone: +4535336131

Email: vito.fodera@sund.ku.dk

Author Contributions :

I.B: Designed research, performed research, analysed data, wrote the paper**, S.L:** Designed research, performed research, analysed data, wrote the paper**, M.P:** Designed research, performed research, analysed data, wrote the paper**, H.A:** Designed research, performed research, analysed data, revised the paper**, R.S:** Performed research, analysed data, revised the paper**, A.H:** Designed research, performed research, analysed data, revised the paper**, M.N.P:** revised the paper**, J.S.M:** Revised the paper**, N.L:** Revised the paper**, F.H.T:** Contributed new reagents/tools**, A.E.T:** Contributed new reagents/tools, revised the paper**, T.P.J.K:** Contributed new reagents/tools**,** revised the paper**, M.G:**, Designed research, revised the paper, acquired funding**, V.F:** Designed research, revised the paper, acquired funding

Competing Interest Statement: A.H, N.L, M.N, J.S.M and M.G are employees of Novo Nordisk A/S.

Classification: Biological Sciences, Biophysics and Computational Biology

Keywords: antibody development, patchy interactions, liquid-liquid phase separation, opalescence, aggregation

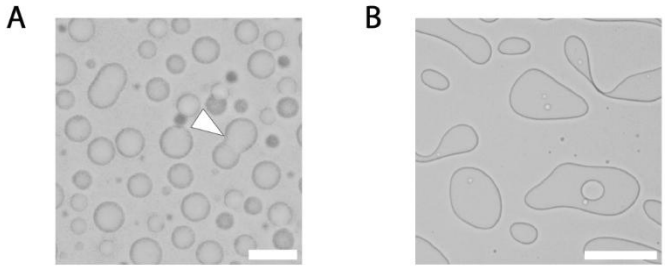

Figure S1: mAb1 LLPS is liquid-like. Brightfield microscopy images of a 45 mg/mL mAb1 sample containing 10 mM NaCl at pH 6.5. The resulting phase-separated droplets are highly dynamic: (A) They fuse and readily coalesce upon contact as indicated by the white arrowhead (10 µm scalebar) and (B) wet the glass surface of the microscopy slide within seconds, emphasizing their liquid-like nature (100 µm scalebar)

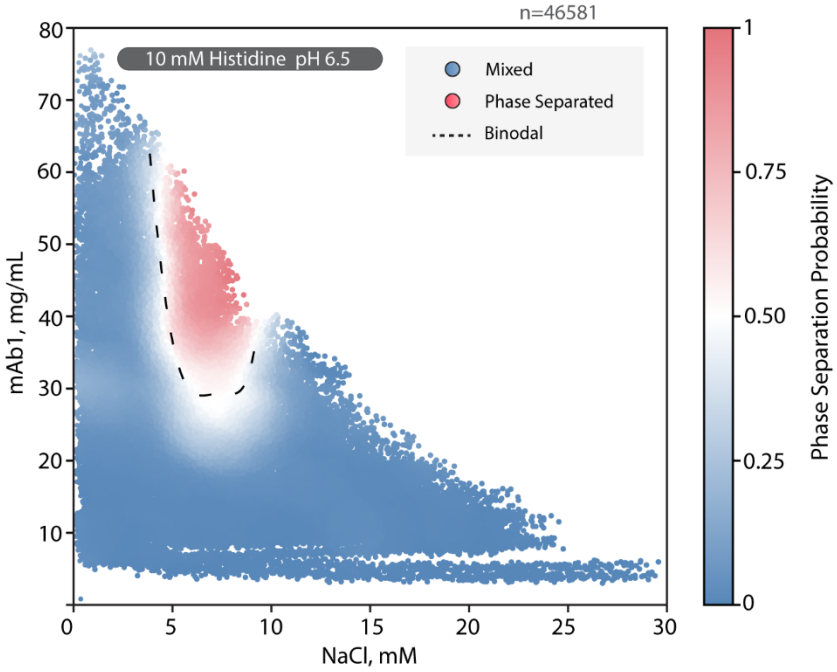

Figure S2: Coexistence curve of mAb1 as a function of NaCl determined using combinatorial microfluidics. Each of the 46581 observations is shaded according to phase separation probability based on local radial averaging. An eye guide for the approximate location of the binodal is indicated by the dashed black line.

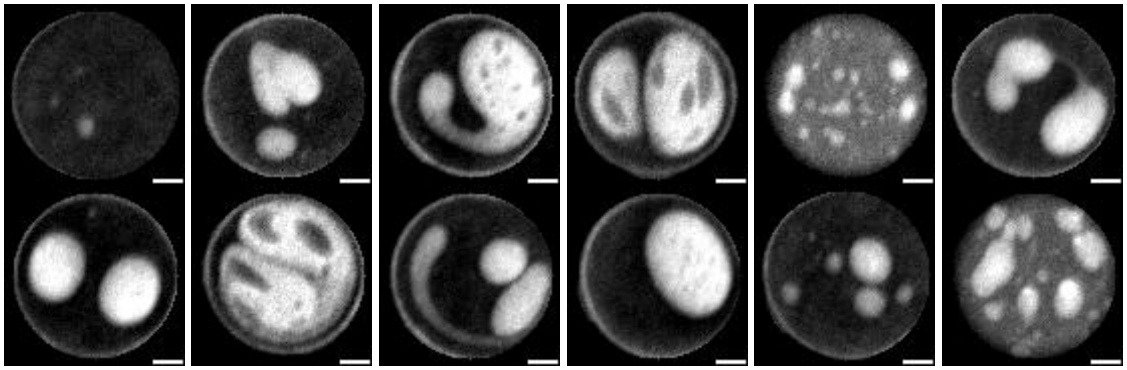

Figure S3: Selected dense phase morphologies detected with PhaseScan using fluorescence microscopy (20 µm scalebar)

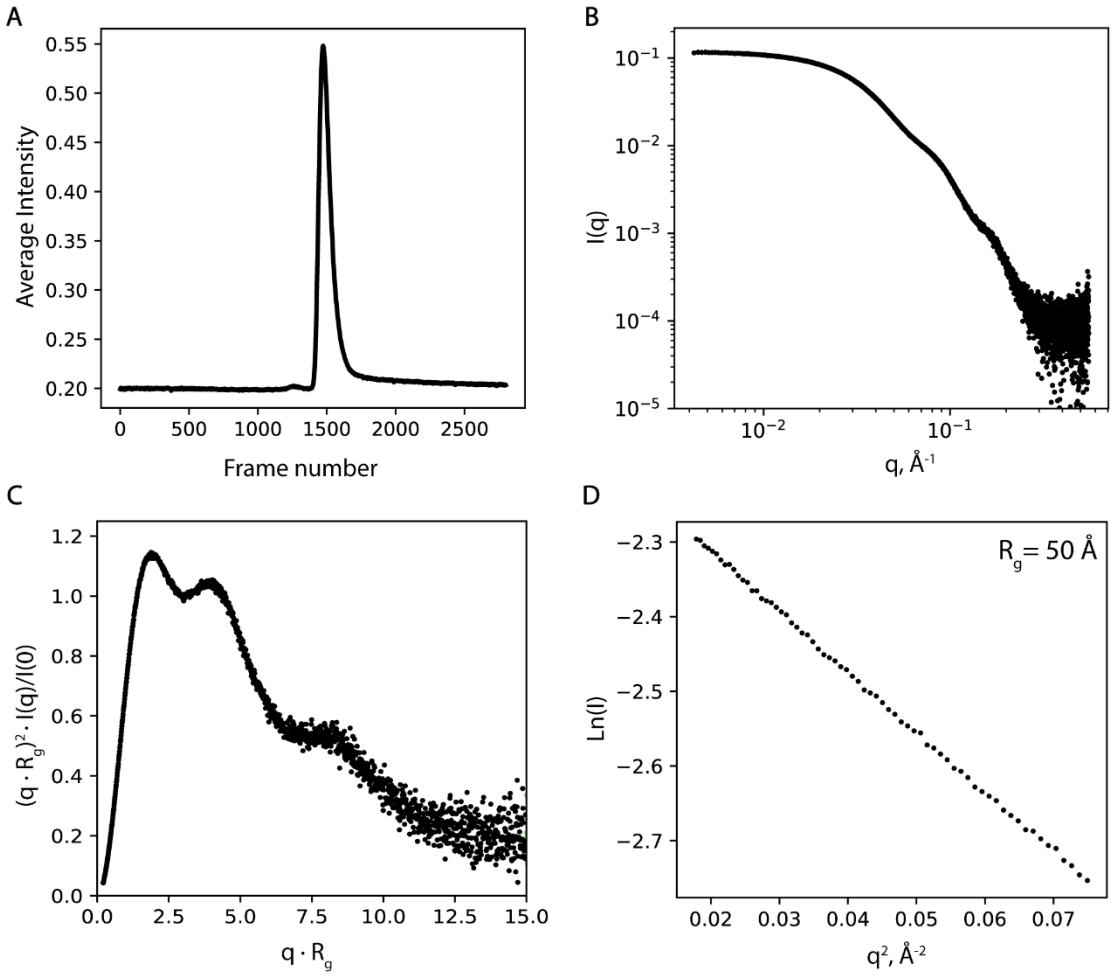

881 **Figure S4: Overview of SEC SAXS measurements of mAb1** (A) Elution profile of 10 mg/mL
882 mAb1 in 10 mM histidine pH 6.5 + 150 mM NaCl mobile phase showing the average integrated
883 SAXS intensity, I(q), ($1.48*10^{-3}$ $Å^{-1}$ < **q** < 0.556 $Å^{-1}$) as a function of frame number (B) Average
884 scattering curve of frames 1454 to 1521, corresponding to monomeric mAb1 (highest peak of the
885 elution profile in A) (C) Dimensionless Kratky plot showing three peaks, as expected for IgG
886 molecules (D) Guinier plot for the monodisperse mAb1 sample showing linearity in the Guinier
887 range and the radius of gyration determined from the slope.

888

889

890

891

892 **Figure S5: Suppression of LLPS and opalescence with L-arginine HCl and effect of stirring**
893 (A) Left: Visual appearance of an LLPS sample containing 45 mg/mL mAb1 in 10 mM histidine, 10
894 mM NaCl, pH 6.5 compared to 45 mg/mL mAb1 in 10 mM histidine, 10 mM NaCl, 150 mM L-
895 arginine-HCl, pH 6.5 (10 mM NaCl+Arg). The latter was added prior to adding the NaCl that would
896 have otherwise made the sample undergo LLPS. Right: Brightfield microscopy of the 10 mM
897 NaCl+Arg sample showing that no LLPS is detected under these conditions. The scalebar
898 represents 50 µm. (B) Same setup as in (A) but with the 22.5 mM (opalescent sample) as well as
899 images of the effect of stirring at 1000 rpm (16 hours), showing the increased visual turbidity of the
900 sample and the presence of aggregates in the microscopy image. The scalebars represents 50 µm.

901

902

903

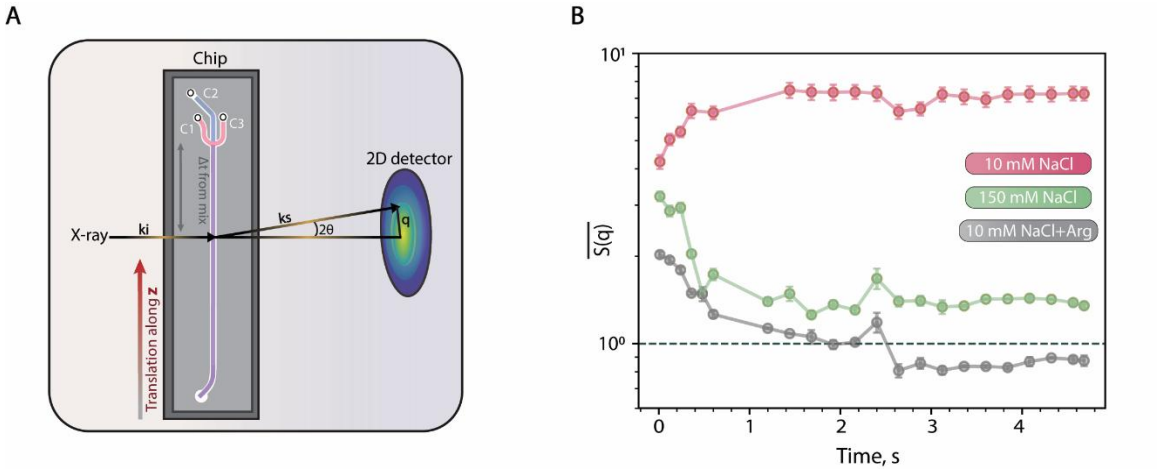

Figure S6: (A) Schematic representation of the microfluidic chip coupled to the Co-SAXS beamline recorded at 22 distances from the mixing point across the channel. The distances were converted to timepoints here. Data was recorded at a total flowrate of 60 µL/min. (B) Averages of the first three S(**q**) values, that is, the first three datapoints at low **q** of each of the 22 curves from the time-resolved experiment, converted to timepoints here.

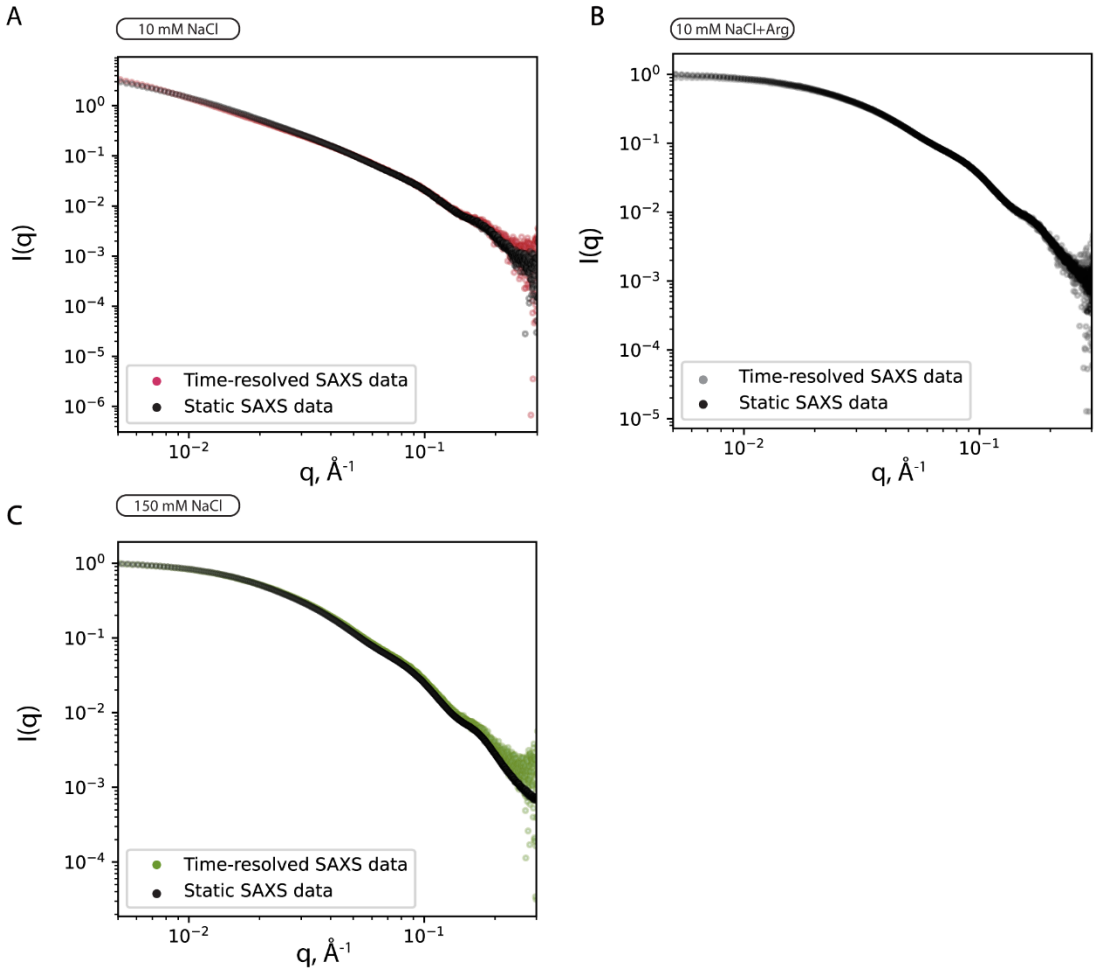

Figure S7: Overlay of the scattering curves (intensity I(**q**) vs **q**) for the last timepoint in the time resolved SAXS experiments (colored curves) and scattering curves from the static SAXS experiment (black curves) for 45 mg/mL mAb1 in 10 mM histidine pH 6.5 containing (A) 10 mM NaCl, (B) 10 mM NaCl + 150 mM arginine HCl (10 mM NaCl+ Arg) or (C) 150 mM NaCl.

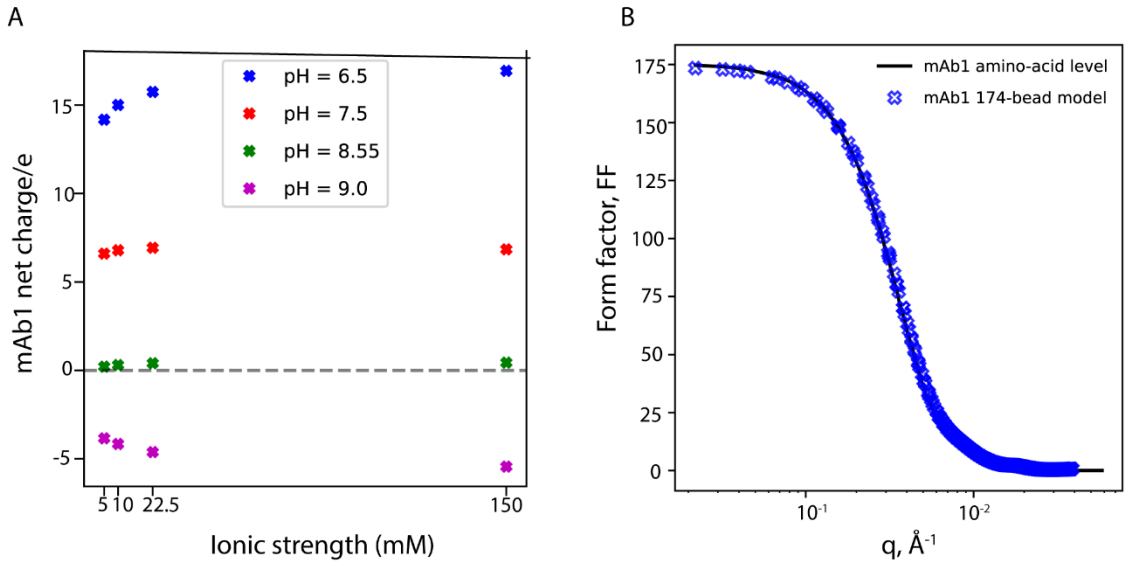

Figure S8: (A) mAb1 net charge in electron units at pH 6.5 (blue), pH 7.5 (red), pH 8.55 (green), and pH 9.0 (purple) as a function of solution IS. (B) mAb1 form factor comparison between the structure coarse-grained at the amino acid level (blue full line) and the 174-bead model (blue symbols).

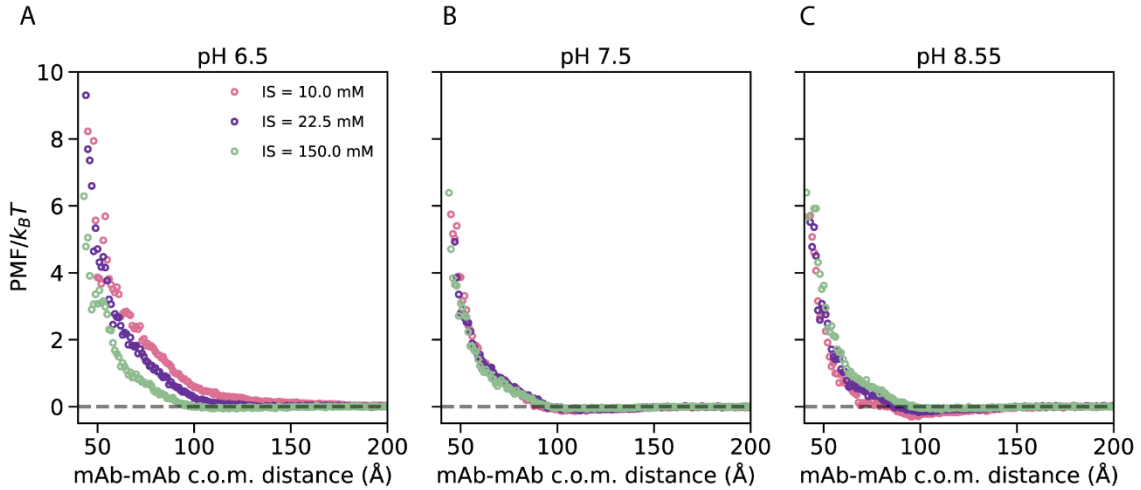

Figure S9: PMF analysis. MAb1 PMF for pH (A) 6.5, (B) pH 7.5, and (C) pH 8.55, for ionic strength conditions of 10 mM (pink), 22.5 mM (purple), and 150 mM (green). Here, ε_{ij} was set to 0.15 kJ/mol to simulate a mild attraction between mAbs.

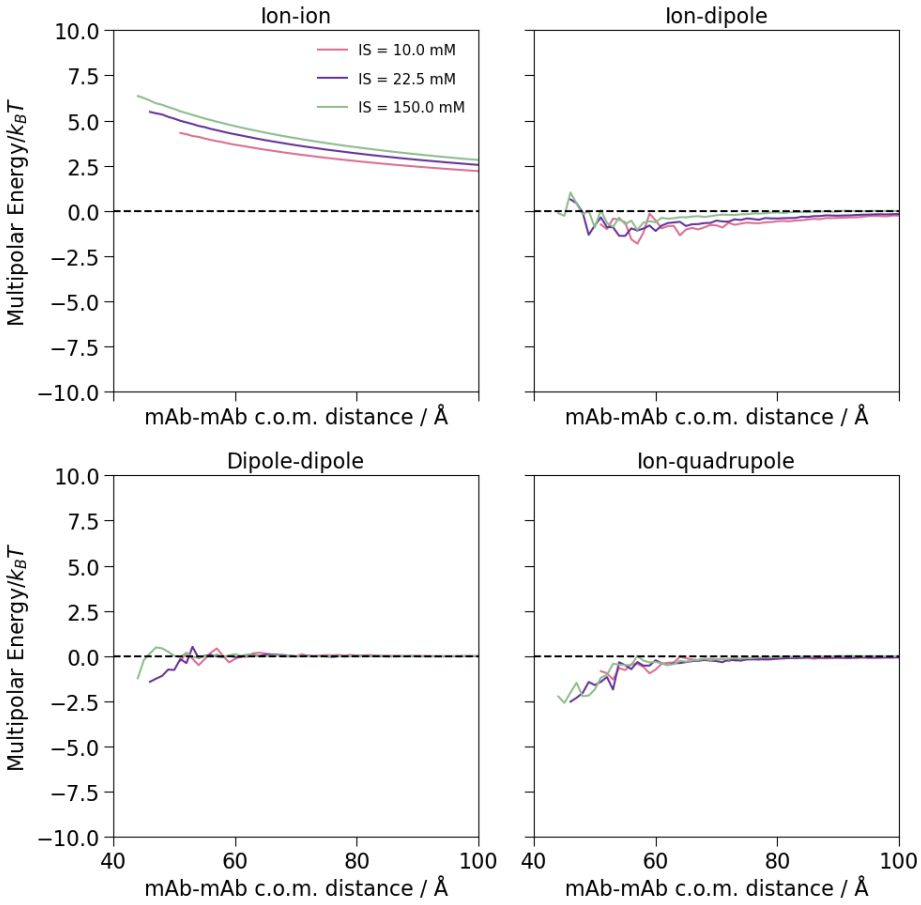

Figure S10: mAb1 multipole expansion contributions for pH = 6.5 resulting from two-mAb simulation where ε_{ij} was set to 0.15 kJ/mol to simulate a mild attraction between mAbs.

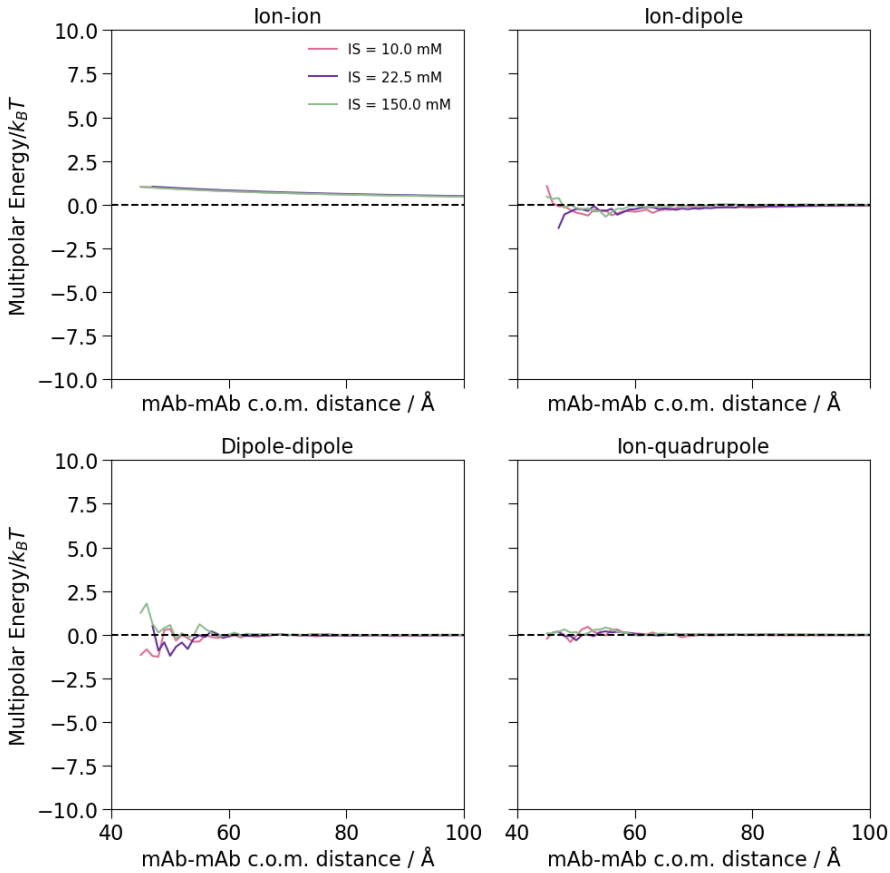

Figure S11: mAb1 multipole expansion contributions for pH = 7.5 resulting from two-mAb simulation where ε_{ij} was set to 0.15 kJ/mol to simulate a mild attraction between mAbs.

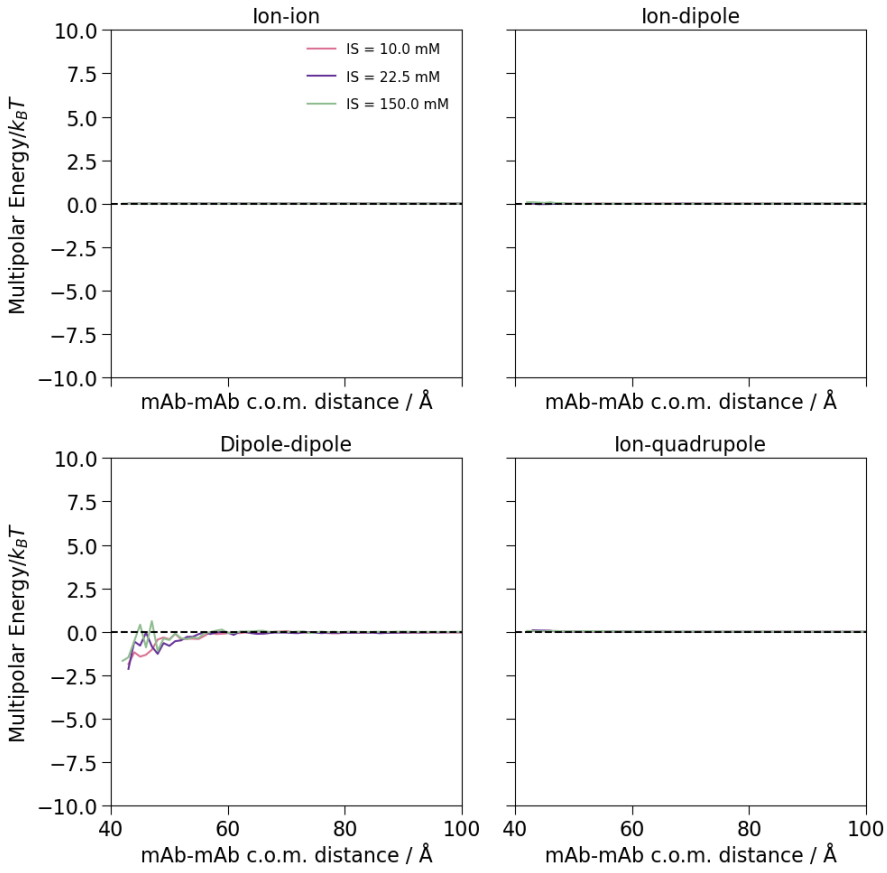

Figure S12: mAb1 multipole expansion contributions for pH = pI = 8.55 resulting from two mAb simulation where ϵij was set to 0.1 kJ/mol to simulate a mild attraction between mAbs.

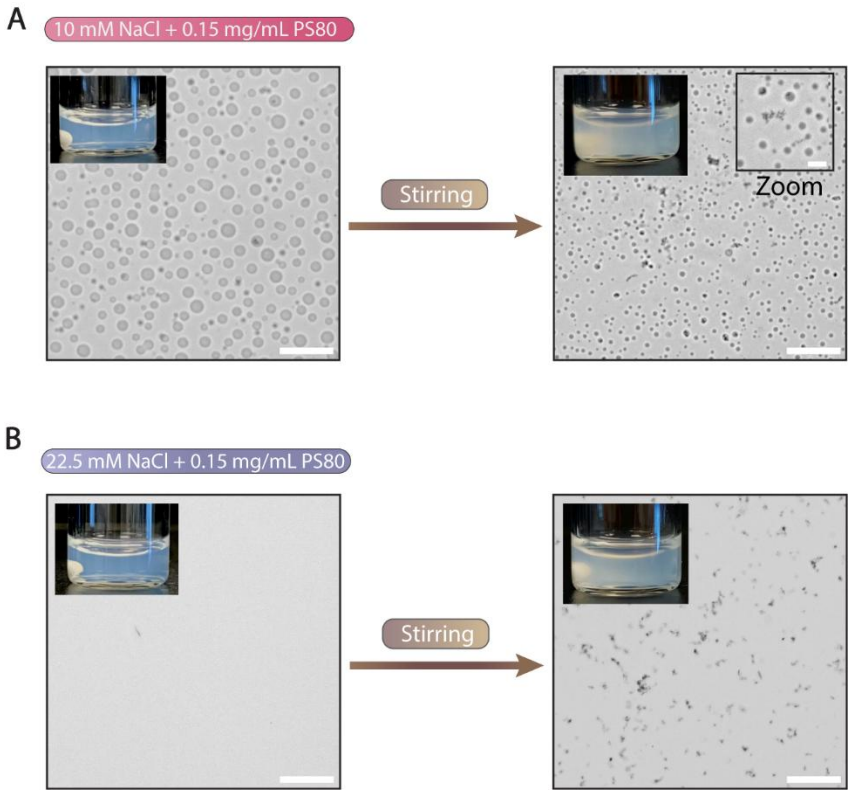

Figure S13: Effect of PS80 on the stirring induced aggregation (A) Visual appearance and brightfield microscopy images of 45 mg/mL mAb1 in 10 mM histidine pH 6.5 containing 10 (A) or 22.5 (B) mM NaCl with 0.15 mg/mL PS80 added. The left images are before stirring and the images on the right are after overnight stirring as described in the methods section. The scalebar represents 50 µm in the main microscopy image and 10 µm in the inset zoom image. In the 10 mM NaCl + 0.15 mg/mL PS80 images, the difference in droplet size arises from their fast dynamics and difference in times at which the images were acquired.

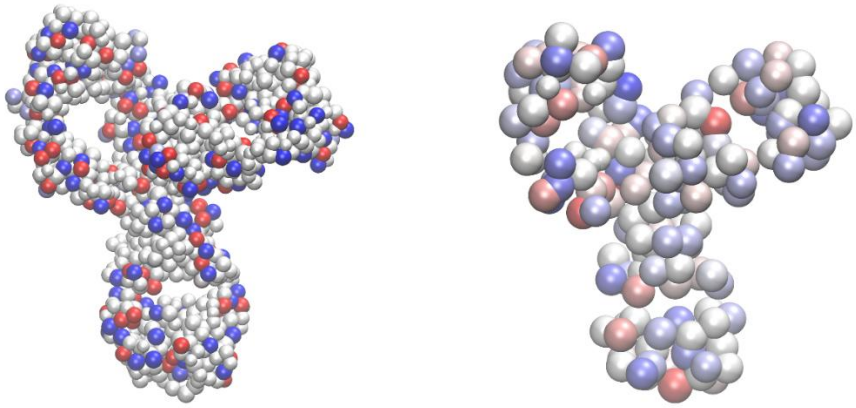

Figure S14: mAb1 coarse-grained models. Amino-acid level (left), and 174-bead model (right). Blue, red, and grey beads represent, respectively, positively, negatively, and neutral charged beads. The current representation reflects the protonation state of the mAb in a solution with 10 mM of NaCl and pH 6.5.

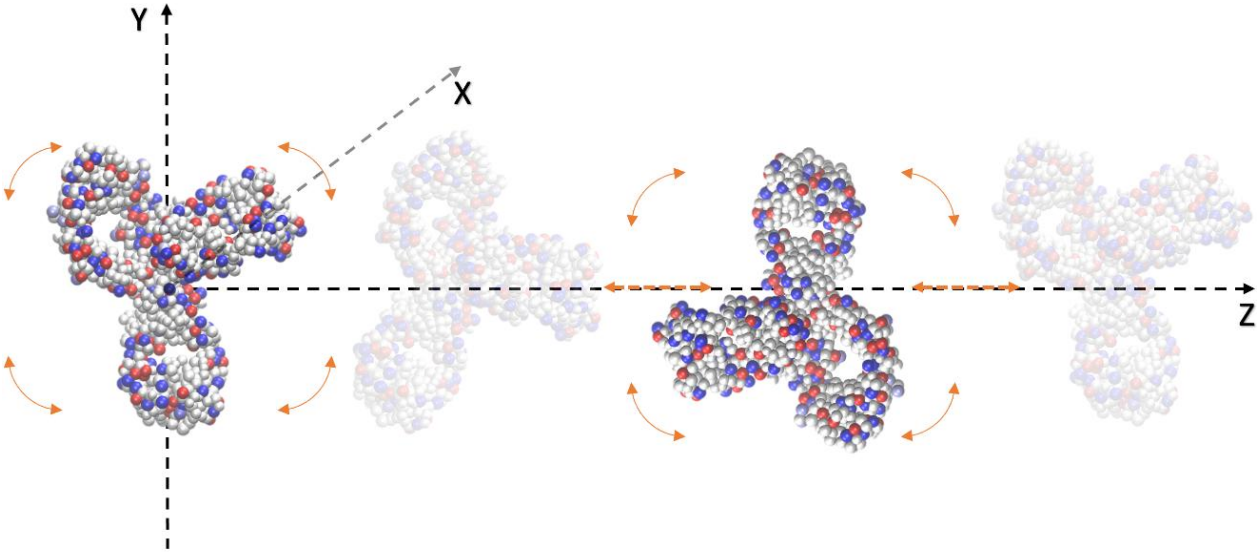

Figure S15: Two-mAb simulations setup. A first mAb (on the left) is placed in the center of the simulation box and can only rotate around its center of mass. A second mAb (on the right) can rotate around its center of mass and rigidly translate along the Z-axis. By sampling different relative positions of the mAbs' center of masses on the z-axis, we sample the radial distribution function, g(r), and consequently, from equations 4 and 5, the PMF and the reduced second osmotic virial coefficient, B_2^*.

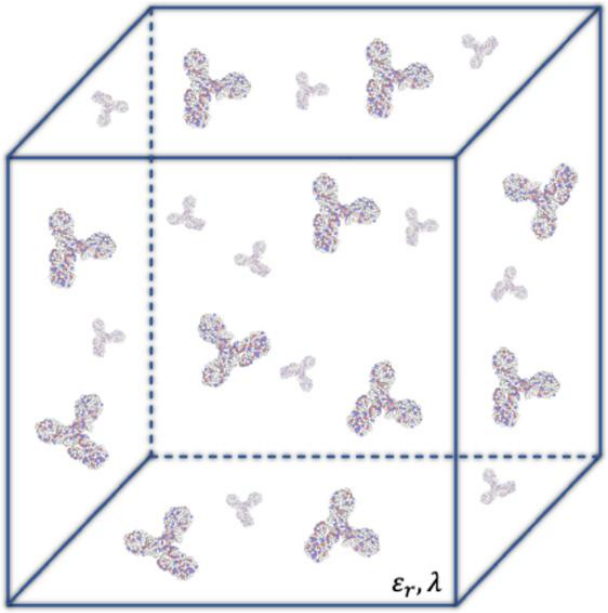

Figure S16: Schematic representation of many-mAb simulations. Inside the simulation box, mAbs can rigidly rotate and translate in all directions. Solvent and salt screening effect are treated implicitly in the interaction potential through the dielectric water constant ε_r, and the Debye length, λ, respectively (see equation 2).

Bead	Sigma	Bead	Sigma
CTR	3.13	TRP	6.95
HCTR	3.13	GLY	4.69
NTR	2.99	ARG	6.50
HNTR	2.99	HARG	6.50
ALA	5.02	LYS	6.05
ILE	5.80	HLYS	6.05
LEU	5.80	ASP	5.94
MET	6.16	HASP	5.94
PHE	6.41	LASP	5.94
VAL	5.56	GLU	6.16
PRO	5.56	HGLU	6.16
SER	5.39	LGLU	6.16
THR	5.64	GLN	6.12
TYR	6.65	ASN	5.91
HTYR	6.65	HIS	6.29
CYS	5.72	HHIS	6.29
HCYS	5.72	GLC	6.62
CYX	5.72		

TABLE S1: Bead name and corresponding sigma values for the mAb1 coarse-graining at the amino acid level.